Helium isotopes and olivine geochemistry of basalts and mantle xenoliths in Jeju Island, South Korea: Evaluation of role of SCLM on the Cenozoic intraplate volcanism in East Asia

Donghwan Kim[a], Hyunwoo Lee[a,*], Wonhee Lee[a], Jonguk Kim[b], Jihye Oh[a,b], Jung-Hun Song[a] Haemyeong Jung[a], Finlay M. Stuart[c]

[a]School of Earth and Environmental Sciences, Seoul National University, Seoul 08826, Republic of Korea

[b]Deep–Sea and Seabed Mineral Resources Research Center, Korea Institute of Ocean Science and Technology, Busan 49111, Republic of Korea

[c]Scottish Universities Environmental Research Centre, East Kilbride G75 0QF, United Kingdom

*Corresponding author.

E-mail address: lhw615@snu.ac.kr (H. Lee).

Keywords: East Asia, Jeju Island, Helium isotopes, Olivine chemistry, Intraplate volcanism, SCLM

Abstract

Jeju Island, South Korea, is a Cenozoic intraplate volcano located in East Asia. The Jeju basalts display ocean island basalt (OIB)-like trace element patterns and enriched mantle type 2 (EM2) radiogenic isotope compositions, but the source that enriched the mantle remains unclear. Here we report new geochemical compositions of basalts and xenoliths, including the first helium isotope and element analysis of olivine phenocrysts to constrain the source of basalt. Olivines in the Jeju basalts have $^3He/^4He$ ratios of 3.5 to 7.3 R_a while olivines in the mantle xenoliths are 2.9 to 6.3 R_a. They provide no evidence of a lower mantle plume but overlap the range of the regional subcontinental lithospheric mantle (SCLM) and OIBs with low $^3He/^4He$ values. Olivine phenocrysts included in the basalts show variations in Mn, Ni, and Ca concentrations with forsterite (Fo) contents, similar to the trend for olivines crystallized from the pyroxenite-derived melts. Elemental ratios of Ca-Fe-Ni-Mg-Mn for the olivines also indicate the pyroxenite contribution. Considering our results, it is suggested that the main source of the Jeju basalts is the SCLM containing pyroxenite. In addition, the tomography image shows the low-velocity zone extending to the asthenosphere mantle beneath the central Jeju Island. This implies that the localized asthenospheric upwelling is caused by edge-driven convection, and the high-velocity zones exist around Jeju island indicating a thick cratonic lithosphere. Therefore, we propose that the interaction between the SCLM component containing pyroxenite and the rising asthenosphere is the main mechanism to generate enriched basaltic magmas for the Cenozoic intraplate volcanism in East Asia, including Jeju Island.

1. Introduction

East Asia, including the Korean Peninsula, mainland China, and adjacent seas, is located on the Eurasian Plate and records extensive Cenozoic intraplate volcanism (Fig. 1a). Although trace element and radiogenic isotope compositions (e.g., Sr, Nd, Pb, and Hf) of the lavas are typical ocean island basalt (OIB) compositions (Chen et al., 2007; Choi et al., 2006; Kimura et al., 2018), there is little consensus on the ultimate origin of this magmatism. Most of the basaltic volcanism in this area appear to display mixing between the depleted mantle (DMM) and the EM1 and EM2 enriched mantle components (Choi et al., 2006). There is a broad geographic distinction in the enriched mantle contribution; the melting beneath northeastern China contains EM1-type enriched mantle while the intraplate volcanism of Southeast Asia is sourced in mantle contaminated by the EM2 component (Choi et al., 2006). However, processes such as the role of lower mantle plume, contribution from the stagnant slab beneath East Asia, and small local convection in the asthenosphere have been extensively discussed, but there is no clear agreement yet (Brenna et al., 2015; Choi et al., 2006; Kimura et al., 2018; Kuritani et al., 2019; Song et al., 2018; Tatsumi et al., 2005; Xu et al., 2017; Zhao et al., 2009). Among the arguments, the metasomatized subcontinental lithospheric mantle (SCLM) has been proposed as the source of continental basalts in East Asia (Guo et al., 2020; Xu et al., 2017) as well as Australia, East Africa, and West Antarctica (Lu et al., 2020; Nardini et al., 2009; Niu, 2008; Pilet et al., 2008; Rooney, 2020). Regarding the East Asian SCLM, it is suggested that it has experienced thinning/delamination of the ancient cratonic lithosphere during the Late Jurassic-Early Cretaceous, subduction-related metasomatism during the Late Cretaceous-Early Cenozoic, and the lithospheric thinning since the Early Cretaceous (Correale et al., 2016; Guo et al., 2014; Liu et al., 2019; Ma et al., 2019; Woo et al., 2014; Xu, 2002; Yamamoto et al., 2004).

In order to test the prevailing hypotheses, we report a study of Jeju Island, a large Cenozoic intraplate volcanic center in the Korean Strait (Brenna et al., 2012a; Koh et al., 2013). According to previous studies (Choi et al., 2006; Kim et al., 2019; Tatsumi et al., 2005), trace element patterns are similar to the OIB trend, and radiogenic isotope compositions (Sr, Nd, Hf, and Pb) show the DMM-EM2 mixing relationship, like basalts reported in southeast Asia. In a recent study (Kim et al., 2019), it has been suggested that the Jeju magma source is likely garnet peridotite but contains recycled components such as rutile bearing eclogite, carbonate, and sedimentary components. Lower mantle, asthenosphere, and SCLM components have been proposed for the origin of the Cenozoic magmatism in East Asia (Brenna et al., 2015; Choi et al., 2006; Kimura et al., 2018; Tatsumi et al., 2005). Also, it has been presented that the stagnant Pacific plate slab beneath this region played an important role in the genesis of enriched magmas (Choi et al., 2006; Kim et al., 2019). The Jeju basalts were reported to have different radiogenic isotope (Sr, Nd, and Pb) compositions compared to peridotite xenoliths, suggesting that magma has been enriched regardless of the contribution of the lithosphere (Baek et al., 2014; Choi et al., 2006). However, pyroxenite segregates in the metasomatized SCLM are typically enriched, and subducted crustal components were stored in the lithosphere in the form of pyroxenite, which contributed to the source of magma through tectonic reactivation (Lu et al., 2020).

Helium isotope ratios ($^3He/^4He$) are powerful for tracking the role of deep mantle and SCLM in intraplate volcanism. The lower mantle likely has $^3He/^4He$ > 50 R_a (e.g., Stuart et al., 2003) while the SCLM is typically lower (6 ± 1 R_a; e.g., Gautheron and Moreira, 2002) than depleted upper mantle (DMM) that melts beneath mid-ocean ridges (8 ± 1 R_a; Graham, 2002). Here we report the first analysis of the helium isotope compositions of young (< 100 ka) basalts and mantle xenoliths from Jeju Island. These are combined with major and trace element compositions of whole rocks and olivine phenocrysts to understand the characteristics of the magma source.

2. Geological setting

Jeju Island, South Korea, is a Cenozoic intraplate volcano located in the Korea Strait, 650 km from the Nankai Trough, the nearest convergent margin (Fig. 1). The subducting slab of the Philippine Sea Plate is not present beneath Jeju (Wei et al., 2015). A stagnant slab of the detached Pacific Plate has been detected in the mantle transition zone (MTZ) beneath the Korea Strait (Huang and Zhao, 2006; Wei et al., 2015) although a more recent full-waveform seismic tomography and P-wave anisotropic tomography study did not detect it (Ma et al., 2019; Tao et al., 2018). The East Asian SCLM has experienced lithospheric thinning since the Early Cretaceous likely caused by the subducting Pacific plate (Correale et al., 2016; Guo et al., 2014; Liu et al., 2019). Jeju Island sits on the continental crust (24.8 to 35 km) which is significantly thinner than the Korean Peninsula and East China (Kim et al., 2015; Yoo et al., 2007). The lithospheric thickness is estimated to be about 60 km beneath the central part of Jeju Island but thickens to the north, west, and east (Song et al., 2018).

Mt. Halla is the central volcanic edifice of Jeju. Volcanism in the past 0.1 Ma has been generated from about 300 scoria cones which are widely distributed across the island (Fig. 1b). The volcanic activity of Jeju is mainly divided into submarine (1.88 Ma to 0.5 Ma) and subaerial periods (0.5 Ma to Holocene), separated by the hydrovolcanic activity of the Seoguipo Formation (Koh et al., 2013). During the subaerial period (Stage 1 of Brenna et al., 2015), the melt flux was relatively low, and both high Al alkaline basalts and trachytic lava flows erupted (Brenna et al., 2015, 2012b). During the subaerial period, the eruption rate increased, forming the current morphology of the island (Brenna et al., 2015). The subaerial period is divided into two stages; stage 2 (500-250 ka) and stage 3 (< 250 ka) (Brenna et al., 2015). Stage 2 is characterized by the transitional alkaline basalts. During stage 3, low-Al alkali basalts erupted dominantly as tholeiites in the western and eastern areas, and continued into historical times (Lee and Yang, 2006).

3. Samples and analytical methods

In this study, we have analyzed fresh stage 3 basalts from the Daepo-Dong (DB) region in the south, Sinchang-Ri (SB) in the west, and Kwideok-Ri (KB) in the northwest of Jeju, respectively (Fig. 1). We also collected mantle xenolith fragments hosted in basaltic rocks from Sinsan-Ri (SX) in east Jeju (Fig. 1). The DB samples are low-Al alkaline basalts, while rocks from SB and KB are tholeiitic basalts (Brenna et al. 2012b; Koh et al. 2013). The DB basalts contain olivine, clinopyroxene, and plagioclase phenocrysts while the SB and KB basalts include only olivine phenocrysts. Mantle xenoliths discovered from Jeju Island can be divided into two groups. Group 1 xenoliths are spinel lherzolite and spinel harzburgite, containing Cr-rich clinopyroxene. Group 2 xenoliths are dunite, wehrlite to olivine clinopyroxenite, and olivine websterite to websterite, having Al-Ti-rich clinopyroxene (Choi et al., 2005; Woo et al., 2014; Yang et al., 2012b). In this study, all xenolith samples are protogranular spinel lherzolites composed of olivine, orthopyroxene (enstatite), and clinopyroxene (diopside). The Jeju lherzolites imply that the SCLM was formed during the Paleoproterozoic (2.1 to 1.8 Ga) according to Os T_{RD} ages and experienced subduction-related metasomatism (Lee and Walker, 2006; Woo et al., 2014). Olivines in the xenoliths have Fo contents of 88.6 to 90.8 (Table 2) typical of upper mantle xenoliths (Choi et al., 2005).

Major element compositions were measured by X-ray fluorescence spectrometry (Shimadzu

XRF-1800) at the Cooperative Laboratory Center, Pukyong National University, Republic of Korea. Mineral grains were epoxy-mounted and major elements were measured by a field emission electron probe microanalyzer (FE-EPMA, JXA-8350F, JEOL) at the National Center for Interuniversity Research Facilities (NCIRF) of Seoul National University, Republic of Korea. Operating conditions were 15 kV accelerating voltage and 20 nA beam current with a beam spot size of 3μm. The reproducibility of the data was verified using the Smithsonian standards (olivine; NMNH 111312-44, augite; NMNH 164905, and chromite; NMNH 117075), with the reproducibility of major elements (RSD%) less than 1.2 % except for FeO (2.65 %) in augite (Supplementary data; Table S3).

Trace element concentrations of whole-rock and mineral grains were measured by LA-ICP-MS (NWR 193 laser ablation system coupled to Agilent 7000x Inductively Coupled Plasma Mass Spectrometer) at Korea Institute of Ocean Science and Technology (KIOST), Republic of Korea. The analysis was performed with output energy of 3 J/cm^2 and a repetition rate of 5 Hz, with a spot size of 105 μm for each run for 40 seconds. The LA-ICP-MS analysis set the same points as the EPMA targets for mineral grains to be used with the FE-EPMA results and internal standards. NIST 612 was used for an external standard, and BCR-2G was used as a secondary external standard to verify accuracy and precision. The Iolite 4 software was used to reduce the amount of trace elements in samples from raw data. Internal standards included Ca in clinopyroxene and the basalt beads, Si in orthopyroxene and olivine, and Cr in spinel, measured by XRF and FE-EPMA. In the secondary external standard (BCR-2G), excluding Zn, accuracy, and precision (RSD%) of most trace element concentrations were better than 17 and 8%, respectively, and the amount was measured between 33 and 56% higher than original amounts (Supplementary data; Table S4).

The basalts and mantle xenoliths were crushed using titanium alloy mortar, sieved and 1-3 mm olivine and clinopyroxene were picked under a binocular microscope. The grains were cleaned with distilled water using Ultrasonicator then ethyl alcohol. Helium isotope compositions ($^3He/^4He$) were measured at Noble Gas Isotope Laboratory, Scottish Universities Environmental Research Centre (SUERC), from gases extracted from melt/fluid inclusions by in vacuo crushing in a hydraulic press. Gas purification procedures are similar to those described previously (Williams et al., 2005). Helium isotope composition was determined using a ThermoFisher Helix-SFT mass spectrometer (Carracedo et al., 2019). The sensitivity and mass fractionation of the mass spectrometer were determined by repeated analyses of the HESJ International standard (Matsuda et al., 2002).

4. Results

Major and trace element compositions of whole rocks are summarized in Table 1 and plotted in Fig. 2. As reported in previous studies on Jeju Island (Baek et al., 2014; Brenna et al., 2015; Tatsumi et al., 2005), the alkaline and subalkaline basalts belong to the low-Al alkaline and tholeiitic types based on SiO_2 and Al_2O_3 contents, respectively (Fig. 2b). The Ti-Mn-P diagram shows that the Jeju basalts fall in the oceanic island basalt (OIB) and oceanic island tholeiite (OIT) fields (Fig. S1). CI chondrite-normalized rare earth element (REE) abundances display light rare earth element (LREE) enriched trends, similar to the typical OIB pattern (Fig. 3a), while primitive mantle normalized trace element patterns are also similar to the OIB trend (Fig. 3b). The trace element patterns of the Jeju basalts are distinguished from the continental crust trend, exhibiting enrichment of large ion lithophile elements (LILE) without depletion of high field strength elements (HFSE). This may indicate that there is no role for metasomatism caused by subduction-related fluids in the mantle source (Fig. 3b).

The major and minor element contents of the Jeju xenoliths (Table 2) are homogenous and similar to those previously reported for Jeju Island and East China (Choi et al., 2005; Correale et al., 2016; Su et al., 2014; Woo et al., 2014). The REE patterns of clinopyroxenes in the Jeju xenoliths are generally spoon-shaped (Fig. 4), with relatively flat trends of the middle (MREE) and heavy rare earth elements (HREE). In addition, both LREE-depletion (SX-01 and SX-04) and LREE-enrichment (SX-02) are observed (Fig. 4). These various LREE enrichments represent various degrees of metasomatism. Furthermore, most of the xenoliths exhibit Nb-Ta depletion with U-Th enrichment (Fig. 4), and Woo et al. (2014) argued that subduction-related fluids may have affected the lithosphere.

The $^3He/^4He$ ratios of the Jeju basalts range from 3.5 to 7.3 R_a (Table 5). There is no clear correlation between the $^3He/^4He$ ratios and He concentrations, nor any systematic differences in $^3He/^4He$ of co-genetic olivine and clinopyroxene (Fig. 5). The $^3He/^4He$ ratios of olivines in the xenoliths extend to slightly lower values but largely overlap the basalt values (2.9 to 6.5 R_a). The absence of any relationship between $^3He/^4He$ and He concentration rules out post-eruptive He ingrowth. The $^3He/^4He$ ratios have a distinctly narrower range than the East Asian SCLM range (Korean Peninsula; 0.2 to 7.9 R_a, North China Craton; 2 to 10.5 R_a, Yangtze Craton; 3.01 to 9.15 R_a, and Far East Russia; 0.3 to 8 R_a) (Correale et al., 2016; Kim et al., 2005; Tang et al., 2014; Yamamoto et al., 2004). This may reflect a lower degree of heterogeneity in the mantle beneath Jeju. The crushing technique used in this study releases less than 0.1% of any radiogenic and cosmogenic He in the mineral lattice (Carracedo et al., 2019). However, other approaches could release lattice-hosted radiogenic and cosmogenic He (e.g., Sumino et al., 2000; Tang et al., 2014). Consequently, the narrower $^3He/^4He$ range that we report might also reflect the absence of released radiogenic and cosmogenic He that seemed to be present in other studies.

The olivine phenocrysts in the Jeju basalts have Fo contents ranging from 69.6 to 79.7 (Table 3). These are lower than typical primary magma compositions, likely reflecting fractional crystallization prior to eruption. The variations of Mn, Ni, and Ca with Fo values are similar to other olivine phenocrysts of basalts from North China and Hainan (Fig. 7). These element contents show small ranges in the same Fo values and good correlations with Fo contents, implying that fractional crystallization is the key process rather than source lithology, mantle temperature, and crystallization pressure (Rasmussen et al., 2020; Sobolev et al., 2007).

5. Discussion

5.1. Crustal assimilation

The assimilation of the radiogenic He-bearing crustal basement by the basaltic magma is likely to lower the initial magmatic $^{3}He/^{4}He$ ratio. However, the deep crystallization of olivines prior to their long period of residence in the continental crust means that, despite evidence of contamination in basalt chemistry or isotopic composition, they can be almost immune to crustal contamination (e.g., Stuart et al., 2003). The basement beneath Jeju Island consists of Jurassic-Early Cenozoic granite and Paleo-Proterozoic anorthosite (Baek et al., 2014; Choi et al., 2006; Kim et al., 2019; Tatsumi et al., 2005), both of which are expected to be concentrated with radiogenic ^{4}He. The trace element compositions of the Jeju basalts yield no strong evidence for crustal contamination, for example, enrichment of LILE (e.g., Rb, Ba, Th, and U) or depletion of HFSE (e.g., Nb, Ta, and Ti) and Sr-Nd-Pb-Mg isotope compositions (Kim et al., 2019; Tatsumi et al., 2005). The Ce/Pb and Nb/U ratios for the basalts are slightly lower than the OIB-MORB ranges (Hofmann et al., 1986) and are close to the upper continental crust ratios (Rudnick and Gao, 2003) (Fig. 6a, b). However, the Th/Nb ratios are relatively uniform compared to the La/Sm ratios (Fig. 6c), and there is no trend of crustal contamination. Previous studies have shown that low-Al alkaline basalts have no meaningful correlation between radiogenic isotope (Sr-Nd) compositions and SiO_2 contents, which indicate crustal assimilation (Brenna et al., 2012b; Kim et al., 2019; Tatsumi et al., 2005). The slightly lower Ce/Pb ratios of low-Al alkaline basalt samples could reflect source characteristics such as enriched sources of the SCLM, which are not identical to MORB and OIB sources.

Baek et al. (2014) and Kim et al. (2019) suggested that some of the Jeju tholeiitic and high-Al alkaline basalts might be contaminated by anorthosite due to the presence of fragments in the tholeiitic basalts (Baek et al., 2014; Yang et al., 2012a) showing positive anomalies of Sr and Eu as well as positive $^{87}Sr/^{86}Sr$ ratio-Sr concentration trends (Tatsumi et al., 2005; Baek et al., 2014; Kim et al., 2019). Compared to the alkaline basalts, the tholeiitic basalts have relatively high $^{207}Pb/^{204}Pb$ ratios with moderate $^{208}Pb/^{204}Pb$ ratios, which may indicate assimilation with anorthosite (Kim et al., 2019; Baek et al., 2014). Since the elevated $^{87}Sr/^{86}Sr$ and $^{207}Pb/^{204}Pb$ ratios are more remarkable in the western region of Jeju Island compared to other regions (Kim et al., 2019), the tholeiitic samples from western Jeju cannot ignore crustal assimilation. Accordingly, the He isotope compositions from tholeiitic basalt samples can be modified by crustal assimilation. The low $^{3}He/^{4}He$ (3.5 R_a) ratios of basalt SB-01 may be due to the addition of radiogenic ^{4}He. Therefore, the $^{3}He/^{4}He$ ratios of the low-Al alkaline basalts can represent the He isotope signatures of Jeju Island, and only the $^{3}He/^{4}He$ ratios of the low-Al alkali basalts will be discussed in the following sections in order to identify the source of magma.

5.2. Magma sources

The $^3He/^4He$ ratios of the Jeju basalts (5.6 to 7.3 R_a) show no evidence for lower mantle signatures represented by the value of >10 Ra (e.g., Stuart et al. 2003). This tends to refute arguments in favor of a lower mantle plume origin for the hotspot volcanism (Kimura et al., 2018; Tatsumi et al., 2005) and is consistent with the absence of hotspot tracks, topographical expansion, and deep thermal anomalies (Brenna et al., 2012b; Kim et al., 2019; Ma et al., 2019; Song et al., 2018). The Sr-Nd-Pb-Hf isotope compositions of the Jeju basalts are consistent with the incorporation of the EM2-type mantle component in the melt source region (Choi et al., 2006; Kim et al., 2019). Given these backgrounds, there could be two possible causes of low $^3He/^4He$ ratios with EM2 signatures in the Jeju volcanism, (i) enriched asthenosphere mantle or (ii) metasomatized SCLM.

(i) Many OIBs are characterized by low $^3He/^4He$ ratios and are typically ascribed to heterogeneity in the asthenosphere mantle owing to the survival of the enriched components (Day et al., 2015; Day and Hilton, 2011; Hanyu et al., 2014; Jackson et al., 2014; Parai et al., 2009). The northeastern Asian asthenosphere has been metasomatized by fluids released from the Pacific stagnant slab at the depth of the MTZ (Kim et al., 2019; Kuritani et al., 2019, 2011; Zhao et al., 2009). However, it is unlikely that the subducted stagnant slab exists beneath Jeju Island. Recent P-wave anisotropic tomography (Ma et al., 2019) and full-waveform seismic tomography (Tao et al., 2018) show that the subducted Pacific plate is cut off beneath Jeju Island. In addition, the subducted Philippine Sea plate extends to a depth of 300 km and, according to the Vp and Vs tomography, does not reach beneath Jeju Island (Wei et al., 2015).

The trace elements and Sr-Nd-Pb isotope compositions, which reflect the DMM component with minor subducted sediment signatures, have been reported from the back-arc basin basalts (BABB) of the Yamato basin (ODP 797) and the Japan basin (ODP 794) located in the East Sea (Japan Sea) (Chen et al., 2015; Hirahara et al., 2015). It is known that helium in the subducted sediments and the oceanic crust is degassed in the subduction zone, and the recycled materials almost lost the He contents (Staudacher and Allègre, 1988). Most of the BABB samples from the Mariana, Manus, Lau, and North Fiji basins exhibit MORB (8±1 R_a) like helium isotope signatures, excluding deep mantle plume-related samples in the Lau and Manus basins (Hilton et al., 2002). The BABBs from the Southern Okinawa trough have $^3He/^4He$ ratios up to 7.9 R_a, despite their high $^{87}Sr/^{86}Sr$ ratios indicating subducted sediments (Yu et al., 2016). Therefore, it is difficult to explain the low $^3He/^4He$ ratios of the basalts from Jeju Island only with the heterogeneous asthenosphere mantle without the contribution of SCLM sources.

(ii) The Jeju basalts with $^3He/^4He$ ratios of 5.6 to 7.3 R_a overlap the range of the mantle xenoliths (2.9 to 6.5 R_a). These are measurably lower than the depleted upper mantle value sampled by MORB (Graham, 2002), and more characteristics of SCLM (Chen et al., 2007; Correale et al., 2016; Gautheron and Moreira, 2002; Tang et al., 2014; Yamamoto et al., 2004). The trace elements and isotope compositions of the Jeju mantle xenoliths imply that the underlying SCLM has experienced metasomatism due to subduction-related fluids and melts (Kim et al., 2005; Woo et al., 2014). Based on the Mg# values of xenolith olivines, Xia et al. (2020) subdivided the lithosphere mantle underneath China into depleted (Mg# > 92) and fertile (Mg# < 90) regions, showing that the fertile lithosphere exists beneath East China, close to Jeju Island. Olivine grains in the Jeju mantle xenoliths typically have the Mg# values of < 90 consistent with the metasomatized SCLM.

The Jeju xenoliths have three REE patterns: LREE depletion, LREE enrichment, and spoon-shaped (LREE enrichment and MREE depletion) patterns (Fig. 4a). These indicate that the lherzolite xenoliths experienced different degrees of depletion or enrichment. Even other harzburgites and mylonitic lherzolite xenoliths from Jeju Island have more LREE enrichment than lherzolites (Woo et al., 2014). According to the Re-Os isotope compositions of the SCLM beneath the Korean Peninsula, Paleoproterozoic harzburgites (1.9-1.8 Ga) are preserved, and the isotope ratios represent the recent perturbation of Re concentrations in lherzolites (Lee and Walker, 2006). Woo et al. (2014) argued that metasomatism of the SCLM resulted from arc-related fluids because of the secondary orthopyroxene morphology and the presence of phlogopite in the lherzolite xenoliths. Due to the differences in the radiogenic isotopes between the peridotite xenoliths (DMM) with the host basalts (EM2), the SCLM has not been considered the source of the magma, instead, the ancient recycled sediments wandering in the asthenosphere have been preferred as the source of EM2 signatures (Baek et al., 2014; Choi et al., 2006). The Jeju basalt samples do not have any subduction-related signatures found in the Jeju lherzolite xenoliths. All of the xenoliths from Jeju Island are spinel lherzolites, and pyroxenites is thought to be derived from the upper part of the SCLM. However, garnet has not been observed in peridotite and pyroxenite xenoliths which are potentially considered to be the source lithology of the Jeju basalts (Choi et al., 2005; Kim et al., 2019).

Recent mantle tomography studies (Song et al., 2020, 2018) have found that the thick cratonic lithosphere is located around Jeju Island, which could be associated with the East Asian SCLM. In North China Craton, various pyroxenite xenoliths displaying EM1 and EM2 signatures, which are distinct from peridotite xenoliths (DMM), have been sampled and argued as being attributed to recycled crustal materials (Xu, 2002). The metasomatized SCLM could contribute to the basalt source and affect the low $^{3}He/^{4}He$ ratios. However, the highest $^{3}He/^{4}He$ ratio (7.3 R_a) of the Jeju basalts falls in the range of MORB (7 to 9 R_a), which represents the asthenospheric mantle contribution. The radiogenic isotope compositions of the Jeju basalts have a mixing trend between the DMM and EM2 components (Choi et al., 2005; Kim et al., 2019; Tatsumi et al., 2005). Hence, it is probable that the formation of the Jeju magma is mainly due to the interaction between the enriched SCLM and depleted MORB mantle components.

The highest $^3He/^4He$ ratio (6.9 R_a) of the tholeiitic basalt sample (KB-01) falls within the range of the alkali basalts (5.6 to 7.3 R_a) (Fig. 5). Compared to the alkaline basalts, the tholeiitic basalts are less enriched in incompatible elements (Fig. 3) and have higher $^{87}Sr/^{86}Sr$ ratios, lower $^{144}Nd/^{143}Nd$ ratios, and higher Δ7/4 Pb values (Kim et al., 2019; Tatsumi et al., 2005). These differences in the radiogenic isotopes between the tholeiitic and alkaline basalts have been discussed in terms of the different depths of magma formation (Brenna et al., 2012b, 2012a; Tatsumi et al., 2005) or anorthosite assimilation (Kim et al., 2019). Nevertheless, the tholeiitic and alkaline basalts have similar trends in the source lithologies based on the olivine compositions (Figs. 7 and 8) and whole-rock compositions (Kim et al., 2019). Therefore, the tholeiite and alkaline basalts originated from the same source, but the divergence into two different basalt types can be attributed to different degrees of partial melting/fractional crystallization.

5.3. Olivine chemistry of the Jeju basalts

In general, basaltic magmas are formed from the melting of peridotite and pyroxenite components. The pyroxenite component is considered to be related to recycled crustal materials from the subducted slab (Sobolev et al., 2007). For this reason, the pyroxenite-derived melts can be distinguished from the peridotite-derived melts based on the minor and trace element compositions (e.g., Mn, Ca, and Ni) in olivine phenocrysts of basaltic rocks (Foley et al., 2013; Rasmussen et al., 2020). Olivines in the Jeju basalts have Fo contents of 68 to 80, which are lower than the primary mantle olivine values (88 to 92; Foley et al., 2013). Hence, it is necessary to consider the chemical variation according to the Fo content of olivine. The Petrolog program was adopted to examine some effects on magma compositions such as fractional crystallization and crustal assimilation (Rasmussen et al., 2020). The melt components derived from peridotite and pyroxenite were referenced from Walter (1998) and Sobolev et al. (2007). According to Yang et al. (2012a), the depth of the Jeju magma chamber was considered to be the depth of the lower continental crust, and the crustal thickness beneath this region was reported to be 24.8~35 km (Kim et al., 2015; Yoo et al., 2007). Thus, we assumed a situation where the fractional crystallization of olivine, clinopyroxene, and plagioclase occurs at 7 kbar.

The Fo contents of olivines in the Jeju basalts show clear correlations with Mn, Ni, and Ca concentrations (Fig. 7). Although olivines in the low-Al alkaline basalts have lower Fo contents than the tholeiitic basalts, the minor and trace element compositions show similar trends (Fig. 7). In particular, most of the variations in the Mn and Ca contents are similar to the crystallization trend of the pyroxenite melt at 7 kbar (Fig. 7), which can be explained by simple crystallization of the pyroxenite-derived melt. As discussed in section 5.1, crustal assimilation did not significantly contribute to the Jeju basalt composition. Thus, it is appropriate to consider the contents of various elements in olivines mainly in terms of fractional crystallization. The element (Mn, Ni, and Ca) contents and ratios (Mn/Fe, Ni/Mg, Ca/Fe and Ni/(Mg/Fe)/1000) in olivine phenocrysts are used to distinguish melting of pyroxenite or peridotite (Rasmussen et al., 2020; Sobolev et al., 2007; Straub et al., 2008). The variation of Ni with Fo content is closer to the pyroxenite trend rather than the peridotite trend (Fig. 7b), which is similar to the characteristics of the Hainan and North China Craton regions (Gu et al., 2019; Li et al., 2016). As noted by Straub et al. (2008), the high Ni contents in the olivines with low Fo contents may be due to mixing between the more primitive magma and the evolved magma (Fig. 7b). The Mn and Ca contents also display similar trends to olivines crystallized in the pyroxenite-derived melts (Fig. 7).

100*Mn/Fe ratios for all olivine phenocrysts are lower than 1.4, which is distinct from the peridotitic values of 1.6 to 1.8 (Fig. 8) (Sobolev et al., 2007). The Mn/Fe ratio is not related to the variation in Fo content because it is known to be significantly controlled by fractional crystallization (Rasmussen et al., 2020; Sobolev et al., 2007). 100Ca/Fe and 100Ni/Mg ratios are lower than the pyroxenite values owing to fractional crystallization. On the other hand, the corrected Ni/(Mg/Fe)/1000 values for fractional crystallization effects are similar to the pyroxenite range. As a result, we believe that pyroxenite is an important source in the formation of the Jeju magma, showing an agreement with Kim et al. (2019).

5.4. Implications for the Cenozoic intraplate volcanism in East Asia

According to the results of our olivine compositions and previous studies, it appears that the source lithologies of the Cenozoic intraplate volcanism in East Asia, including Jeju Island, are mixtures of garnet peridotite and pyroxenite (Gu et al., 2019; Kim et al., 2019; Li et al., 2016; Yang et al., 2016). The enriched pyroxenite xenoliths have been widely reported in East Asia (Xu, 2002; Xu et al., 2002; Yu et al., 2010). Pyroxenite is a part that stores recycled crustal components and is distributed in SCLM, showing various characteristics of trace elements and radiogenic isotopes, providing information on diverse sources of the East Asian Cenozoic basalts (Xu et al., 2017). In addition, the low $^{3}He/^{4}He$ ratios (5.6 to 7.3 R_a) of the basalts support that the pyroxenite melts in Jeju Island might be derived from the SCLM, unlike the Hawaiian shield basalts showing enriched mantle compositions through eclogite/pyroxenite recycled in the lower mantle (Sobolev et al., 2005, 2007).

The reported noble gas isotope compositions (e.g., He and Ar) of the East Asian xenoliths show a wide range (Fig. 5), indicating the contribution of the crustal components to the SCLM (Correale et al., 2016; Tang et al., 2014; Yamamoto et al., 2004). The ancient East Asian SCLM, including North China Craton and Yangtze Craton, was eroded and delaminated from the

Triassic to the Early Cretaceous and was replaced by the juvenile SCLM since the Late Cretaceous (Gan et al., 2018; Lee and Walker, 2006; Liu et al., 2019). Moreover, it is suggested that the SCLM has been metasomatized by the asthenospheric upwelling possibly due to the lithospheric thinning and delamination of the ancient lithosphere that occurred during the Late Jurassic-Early Cretaceous, or by subduction-related fluids/melts until the Early Cenozoic (Correale et al., 2016; Gan et al., 2018; Liu et al., 2019; Woo et al., 2014; Xu, 2002; Yamamoto et al., 2004).

Pyroxenite stored in the lithosphere has been proposed as a major source of continental basalts occurring not only in East Asia, but also in other continents such as the East Africa Rift, West Antarctica, and Southeastern Australia (LeMasurier et al., 2016; Lu et al., 2020; Rooney, 2020). The stored pyroxenite may be involved in the magma formation by the interaction between the SCLM containing fertile pyroxenite and the asthenospheric melts, which can explain the mixing relationship of the radiogenic isotope compositions between the depleted and enriched mantle components (Xu et al., 2017). Additionally, helium isotope ratios of basalts from East-Central China (0.6 to 7.5 R_a) and Jeju Island (3.5 to 7.3 R_a) are lower and wider than the MORB range (7 to 9 R_a). This can be explained by that the metasomatized SCLM that has a wide range of $^{3}He/^{4}He$ ratios have influenced the East Asian magma formation during the Cenozoic era (Xu et al., 2014).

In Fig. 9, seismic tomography shows a low-velocity zone (LVZ) beneath Jeju Island (Song et al., 2020), indicating localized asthenospheric upwelling. The width of the LVZ increases with depth (Fig. 9 and Fig. S2 for model resolution), and high-velocity zones exist at the depth of SCLM (~55km) in the east, west, north of the Jeju Island, which is attributed to the relatively thick lithosphere of Sino-Korean Craton (Song et al., 2018). Variations in lithospheric thickness could lead to focused asthenospheric upwelling via edge-driven convection (Song et al., 2018;

references therein). The focused LVZ beneath the central part of Jeju Island at a depth of about 60 km represents decompressional melting and intensive interaction between the SCLM and the ascending asthenosphere (Song et al., 2018), resulting in the lithosphere weakening and melting due to thermal perturbation (Rooney, 2020). Therefore, melting of pyroxenite segregates contained in the SCLM by the localized asthenospheric upwelling could produce the Jeju magma (Fig. 10). In Guo et al. (2016) and Song et al. (2020), the Cenozoic volcanic areas in East Asia are thought to be mostly related to the LVZs of the upper mantle, and the heterogeneous lithosphere is observed beneath the Korean peninsula and North China Craton. Thus, taking geophysical observations together with our geochemical results provides a robust model of the interaction between the continental lithosphere and the convective upper mantle.

6. Conclusions

The $^3He/^4He$ ratios of the Jeju basalts and xenoliths are 3.5 to 7.3 R_a and 2.9 to 6.5 R_a, respectively, falling within the range of the East Asian SCLM (0.2 to 10.5 R_a). Most Jeju basalt samples are unlikely affected by the crustal assimilation based on the trace element compositions. Except for SB-01 showing a $^3He/^4He$ ratio of 3.5 Ra (SB-01) possibly due to the addition of radiogenic ^4He from crustal contamination, the $^3He/^4He$ ratios of the Jeju basalts (5.6 to 7.3 R_a) imply that the SCLM played a major role in the formation of magma. Although the HIMU-like plume or the subduction-related mantle wedge can be low $^3He/^4He$ reservoirs, they are excluded by trace element and radiogenic isotope compositions. Also, the wide range of $^3He/^4He$ ratios of the Jeju xenoliths is attributed to the SCLM that was metasomatized by lithospheric thinning/delamination of the ancient lithosphere occurred during the Late Jurassic-Early Cretaceous or subduction-related fluids/melts in the Late Cretaceous to the Early Cenozoic. Our results of olivine geochemistry indicate that the source lithology is a hybrid of pyroxenite and peridotite. In the tomography model (Fig. 9), the LVZ in the asthenosphere beneath Jeju Island can reflect the localized asthenospheric upwelling as edge-driven convection (Song et al., 2018, 2020). The asthenospheric upwelling could enhance the thermal perturbation of the lithosphere, resulting in melting. Considering geochemical data and mantle tomography together, we propose that the enriched Cenozoic East Asian magmas were created by the interaction between the upwelling asthenospheric mantle and the metasomatized SCLM that contained pyroxenite storing crustal components.

Acknowledgments

This study was sponsored by the National Research Foundation of Korea (NRF) grant funded by the Korea government (MSIT) (NRF-2019R1G1A1002297). We appreciate Xian-Hua Li for handling our manuscript as an editor. We also thank Marco Brenna and an anonymous reviewer for their constructive comments to improve our manuscript.

References

Baek, S., Choi, S.H., Lee, S.G., Lee, S.R., Lee, H.M., 2014. Geochemistry of anorthositic xenolith and host tholeiite basalt from Jeju Island, South Korea. Geosci. J. 18, 125–135. https://doi.org/10.1007/s12303-013-0060-9

Brenna, M., Cronin, S.J., Kereszturi, G., Sohn, Y.K., Smith, I.E.M., Wijbrans, J., 2015. Intraplate volcanism influenced by distal subduction tectonics at Jeju Island, Republic of Korea. Bull. Volcanol. 77. https://doi.org/10.1007/s00445-014-0896-5

Brenna, M., Cronin, S.J., Smith, I.E.M., Maas, R., Sohn, Y.K., 2012a. How small-volume basaltic magmatic systems develop: A case study from the jeju island volcanic field, Korea. J. Petrol. 53, 985–1018. https://doi.org/10.1093/petrology/egs007

Brenna, M., Cronin, S.J., Smith, I.E.M., Sohn, Y.K., Maas, R., 2012b. Spatio-temporal evolution of a dispersed magmatic system and its implications for volcano growth, Jeju Island Volcanic Field, Korea. Lithos 148, 337–352. https://doi.org/10.1016/j.lithos.2012.06.021

Carracedo, A., Rodés, Smellie, J.L., Stuart, F.M., 2019. Episodic erosion in West Antarctica inferred from cosmogenic ^{3}He and ^{10}Be in olivine from Mount Hampton. Geomorphology 327, 438–445. https://doi.org/10.1016/j.geomorph.2018.11.019

Chen, Shuang shuang, Liu, J. qi, Chen, Sheng sheng, Guo, Z. fu, Sun, C. qing, 2015. Variations in the geochemical structure of the mantle wedge beneath the northeast Asian marginal region from pre- to post-opening of the Japan Sea. Lithos 224–225, 324–341. https://doi.org/10.1016/j.lithos.2015.03.008

Chen, Y., Zhang, Y., Graham, D., Su, S., Deng, J., 2007. Geochemistry of Cenozoic basalts and mantle xenoliths in Northeast China. Lithos 96, 108–126. https://doi.org/10.1016/j.lithos.2006.09.015

Choi, S.H., Kwon, S.T., Mukasa, S.B., Sagong, H., 2005. Sr-Nd-Pb isotope and trace element systematics of mantle xenoliths from Late Cenozoic alkaline lavas, South Korea. Chem. Geol. 221, 40–64. https://doi.org/10.1016/j.chemgeo.2005.04.008

Choi, S.H., Mukasa, S.B., Kwon, S.T., Andronikov, A. V., 2006. Sr, Nd, Pb and Hf isotopic compositions of late Cenozoic alkali basalts in South Korea: Evidence for mixing between the two dominant asthenospheric mantle domains beneath East Asia. Chem. Geol. 232, 134–151. https://doi.org/10.1016/j.chemgeo.2006.02.014

Correale, A., Rizzo, A.L., Barry, P.H., Lu, J., Zheng, J., 2016. Refertilization of lithospheric mantle beneath the Yangtze craton in south-east China: Evidence from noble gases geochemistry. Gondwana Res. 38, 289–303. https://doi.org/10.1016/j.gr.2016.01.003

Day, J.M.D., Barry, P.H., Hilton, D.R., Burgess, R., Pearson, D.G., Taylor, L.A., 2015. The helium flux from the continents and ubiquity of low-3He/4He recycled crust and lithosphere. Geochim. Cosmochim. Acta 153, 116–133. https://doi.org/10.1016/j.gca.2015.01.008

Day, J.M.D., Hilton, D.R., 2011. Origin of 3He/4He ratios in HIMU-type basalts constrained from Canary Island lavas. Earth Planet. Sci. Lett. 305, 226–234. https://doi.org/10.1016/j.epsl.2011.03.006

Foley, S.F., Jacob, D.E., O'Neill, H.S.C., 2011. Trace element variations in olivine phenocrysts from Ugandan potassic rocks as clues to the chemical characteristics of parental magmas. Contrib. to Mineral. Petrol. 162, 1–20. https://doi.org/10.1007/s00410-010-0579-y

Foley, S.F., Prelevic, D., Rehfeldt, T., Jacob, D.E., 2013. Minor and trace elements in olivines as probes into early igneous and mantle melting processes. Earth Planet. Sci. Lett. 363, 181–191. https://doi.org/10.1016/j.epsl.2012.11.025

Gan, C., Zhang, Y., Barry, T.L., He, J., Wang, Y., 2018. Jurassic metasomatised lithospheric mantle beneath South China and its implications: Geochemical and Sr-Nd isotope evidence from the Late Jurassic shoshonitic rocks. Lithos 320–321, 236–249. https://doi.org/10.1016/j.lithos.2018.09.007

Gautheron, C., Moreira, M., 2002. Helium signature of the subcontinental lithospheric mantle. Earth Planet. Sci. Lett. 199, 39–47. https://doi.org/10.1016/S0012-821X(02)00563-0

Graham, D.W., 2002. Noble gas isotope geochemistry of mid-ocean ridge and ocean island basalts: Characterization of mantle source reservoirs. Rev. Mineral. Geochemistry 47, 247–317. https://doi.org/10.2138/rmg.2002.47.8

Gu, X.Y., Wang, P.Y., Kuritani, T., Hanski, E., Xia, Q.K., Wang, Q.Y., 2019. Low water content in the mantle source of the Hainan plume as a factor inhibiting the formation of a large igneous province. Earth Planet. Sci. Lett. 515, 221–230. https://doi.org/10.1016/j.epsl.2019.03.034

Guo, P., Niu, Y., Sun, P., Gong, H., Wang, X., 2020. Lithosphere thickness controls continental basalt compositions: An illustration using Cenozoic basalts from eastern China. Geology 48, 128–133. https://doi.org/10.1130/G46710.1

Guo, P., Niu, Y., Ye, L., Liu, J., Sun, P., Cui, H., Zhang, Y., Gao, J., Su, L., Zhao, J., Feng, Y., 2014. Lithosphere thinning beneath west North China Craton: Evidence from geochemical and Sr–Nd–Hf isotope compositions of Jining basalts. Lithos 202–203, 37–54. https://doi.org/10.1016/j.lithos.2014.04.024

Guo, Z., Afonso, J.C., Qashqai, M.T., Yang, Y., Chen, Y.J., 2016. Thermochemical structure of the North China Craton from multi-observable probabilistic inversion: Extent and causes of cratonic lithosphere modification. Gondwana Res. 37, 252–265. https://doi.org/10.1016/j.gr.2016.07.002

Hanyu, T., Kawabata, H., Tatsumi, Y., Kimura, J.I., Hyodo, H., Sato, K., Miyazaki, T., Chang, Q., Hirahara, Y., Takahashi, T., Senda, R., Nakai, S., 2014. Isotope evolution in the HIMU reservoir beneath St. Helena: Implications for the mantle recycling of U and Th. Geochim. Cosmochim. Acta 143, 232–252. https://doi.org/10.1016/j.gca.2014.03.016

Hilton, D.R., Fischer, T.P., Marry, B., 2002. Noble gases and volatile recycling at subduction zones. Rev. Mineral. Geochemistry 47. https://doi.org/10.2138/rmg.2002.47.9

Hirahara, Y., Kimura, J.-I., Senda, R., Miyazaki, T., Kawabata, H., Takahashi, T., Chang, Q., Vaglarov, B.S., Sato, T., Kodaira, S., 2015. Geochemical variations in Japan Sea back-arc basin basalts formed by high-temperature adiabatic melting of mantle metasomatized by sediment subduction components. Geochemistry, Geophys. Geosystems 16, 1324–1347. https://doi.org/10.1002/2015GC005720

Hofmann, A.W., Jochum, K.P., Seufert, M., White, W.M., 1986. Nb and Pb in oceanic basalts: new constraints on mantle evolution. Earth Planet. Sci. Lett. 79, 33–45. https://doi.org/10.1016/0012-821X(86)90038-5

Huang, J., Zhao, D., 2006. High-resolution mantle tomography of China and surrounding regions. J. Geophys. Res. Solid Earth 111, 1–21. https://doi.org/10.1029/2005JB004066

Jackson, M.G., Hart, S.R., Konter, J.G., Kurz, M.D., Blusztajn, J., Farley, K.A., 2014. Helium and lead isotopes reveal the geochemical geometry of the Samoan plume. Nature 514, 355–358. https://doi.org/10.1038/nature13794

Kim, J.-I., Choi, S.H., Koh, G.W., Park, J.B., Ryu, J.-S., 2019. Petrogenesis and mantle source characteristics of volcanic rocks on Jeju Island, South Korea. Lithos 326–327, 476–490. https://doi.org/10.1016/j.lithos.2018.12.034

Kim, K.H., Nagao, K., Tanaka, T., Sumino, H., Nakamura, T., Okuno, M., Lock, J.B., Youn, J.S., Song, J., 2005. He-Ar and Nd-Sr isotopic compositions of ultramafic xenoliths and host alkali basalts from the Korean peninsula. Geochem. J. 39, 341–356. https://doi.org/10.2343/geochemj.39.341

Kim, Y.H., Lee, C., Kim, S.S., 2015. Tectonics and volcanism in East Asia: Insights from geophysical observations. J. Asian Earth Sci. 113, 842–856. https://doi.org/10.1016/j.jseaes.2015.07.032

Kimura, J.I., Sakuyama, T., Miyazaki, T., Vaglarov, B.S., Fukao, Y., Stern, R.J., 2018. Plume-stagnant slab-lithosphere interactions: Origin of the late Cenozoic intra-plate basalts on the East Eurasia margin. Lithos 300–301, 227–249. https://doi.org/10.1016/j.lithos.2017.12.003

Koh, G.W., Park, J.B., Kang, B.-R., Kim, G.-P., Moon, D.C., 2013. Volcanism in Jeju Island. J. Geol. Soc. Korea 49, 209–230.

Kuritani, T., Ohtani, E., Kimura, J.I., 2011. Intensive hydration of the mantle transition zone beneath China caused by ancient slab stagnation. Nat. Geosci. 4, 713–716. https://doi.org/10.1038/ngeo1250

Kuritani, T., Xia, Q.K., Kimura, J.I., Liu, J., Shimizu, K., Ushikubo, T., Zhao, D., Nakagawa, M., Yoshimura, S., 2019. Buoyant hydrous mantle plume from the mantle transition zone. Sci. Rep. 9, 1–7. https://doi.org/10.1038/s41598-019-43103-y

Lee, K., Yang, W.S., 2006. Historical seismicity of Korea. Bull. Seismol. Soc. Am. 96, 846–855. https://doi.org/10.1785/0120050050

Lee, S.R., Walker, R.J., 2006. Re-Os isotope systematics of mantle xenoliths from South Korea: Evidence for complex growth and loss of lithospheric mantle beneath East Asia. Chem. Geol. https://doi.org/10.1016/j.chemgeo.2006.01.003

LeMasurier, W.E., Choi, S.H., Hart, S.R., Mukasa, S., Rogers, N., 2016. Reconciling the shadow of a subduction signature with rift geochemistry and tectonic environment in Eastern Marie Byrd Land, Antarctica. Lithos 260, 134–153. https://doi.org/10.1016/j.lithos.2016.05.018

Li, H.-Y., Xu, Y.-G., Ryan, J.G., Huang, X.-L., Ren, Z.-Y., Guo, H., Ning, Z.-G., 2016. Olivine and melt inclusion chemical constraints on the source of intracontinental basalts from the eastern North China Craton: Discrimination of contributions from the subducted Pacific slab. Geochim. Cosmochim. Acta 178, 1–19.

https://doi.org/https://doi.org/10.1016/j.gca.2015.12.032

Liu, J., Cai, R., Pearson, D.G., Scott, J.M., 2019. Thinning and destruction of the lithospheric mantle root beneath the North China Craton: A review. Earth-Science Rev. 196, 102873. https://doi.org/10.1016/j.earscirev.2019.05.017

Lu, J., Tilhac, R., Griffin, W.L., Zheng, J., Xiong, Q., Oliveira, B., O'Reilly, S.Y., 2020. Lithospheric memory of subduction in mantle pyroxenite xenoliths from rift-related basalts. Earth Planet. Sci. Lett. 544, 116365. https://doi.org/10.1016/j.epsl.2020.116365

Ma, J., Tian, Y., Zhao, D., Liu, C., Liu, T., 2019. Mantle Dynamics of Western Pacific and East Asia: New Insights from P Wave Anisotropic Tomography. Geochemistry, Geophys. Geosystems 20, 3628–3658. https://doi.org/10.1029/2019GC008373

Matsuda, J., Matsumoto, T., Sumino, H., Nagao, K., Yamamoto, J., Miura, Y., Kaneoka, I., Takahata, N., Sano, Y., 2002. The $^{3}He/^{4}He$ ratio of new internal He Standard of Japan (HESJ). Geochem. J. 36, 191–195. https://doi.org/10.2343/geochemj.36.191

Nardini, I., Armienti, P., Rocchi, S., Dallai, L., Harrison, D., 2009. Sr-Nd-Pb-H-O isotope and geochemical constraints on the genesis of cenozoic magmas from the West Antarctic Rift. J. Petrol. 50, 1359–1375. https://doi.org/10.1093/petrology/egn082

Niu, Y., 2008. The origin of alkaline lavas. Science 320, 883–884. https://doi.org/10.1126/science.1158378

Parai, R., Mukhopadhyay, S., Lassiter, J.C., 2009. New constraints on the HIMU mantle from neon and helium isotopic compositions of basalts from the Cook-Austral Islands. Earth Planet. Sci. Lett. 277, 253–261. https://doi.org/10.1016/j.epsl.2008.10.014

Pilet, S., Baker, M.B., Stolper, E.M., 2008. Metasomatized Lithosphere and the Origin of

Alkaline Lavas. Science (80-.). 320, 916–919. https://doi.org/10.1126/science.1156563

Rasmussen, M.B., Halldórsson, S.A., Gibson, S.A., Guðfinnsson, G.H., 2020. Olivine chemistry reveals compositional source heterogeneities within a tilted mantle plume beneath Iceland. Earth Planet. Sci. Lett. 531, 116008. https://doi.org/10.1016/j.epsl.2019.116008

Reinhard, A.A., Jackson, M.G., Harvey, J., Brown, C., Koornneef, J.M., 2016. Extreme differences in 87Sr/86Sr between Samoan lavas and the magmatic olivines they host: Evidence for highly heterogeneous 87Sr/86Sr in the magmatic plumbing system sourcing a single lava. Chem. Geol. 439, 120–131. https://doi.org/10.1016/j.chemgeo.2016.05.017

Rooney, T.O., 2020. The Cenozoic magmatism of East Africa: Part V – Magma sources and processes in the East African Rift. Lithos 360–361, 105296. https://doi.org/10.1016/j.lithos.2019.105296

Rudnick, R.L., Gao, S., Holland, H.D. and Turekian, K.K., 2003. Composition of the continental crust. The crust 3, 1–64.

Sobolev, A. V., Hofmann, A.W., Kuzmin, D. V., Yaxley, G.M., Arndt, N.T., Chung, S.L., Danyushevsky, L. V., Elliott, T., Frey, F.A., Garcia, M.O., Gurenko, A.A., Kamenetsky, V.S., Kerr, A.C., Krivolutskaya, N.A., Matvienkov, V. V., Nikogosian, I.K., Rocholl, A., Sigurdsson, I.A., Sushchevskaya, N.M., Teklay, M., 2007. The amount of recycled crust in sources of mantle-derived melts. Science 316, 412–417. https://doi.org/10.1126/science.

Sobolev, A. V., Hofmann, A.W., Sobolev, S. V., Nikogosian, I.K., 2005. An olivine-free mantle source of Hawaiian shield basalts. Nature 434, 590–597. https://doi.org/10.1038/nature03411

Song, J.H., Kim, S., Rhie, J., 2020. Heterogeneous modification and reactivation of a craton margin beneath the Korean Peninsula from teleseismic travel time tomography. Gondwana

Res. 81, 475–489. https://doi.org/10.1016/j.gr.2019.11.016

Song, J.H., Kim, S., Rhie, J., Lee, S.H., Kim, Y.H., Kang, T.S., 2018. Imaging of Lithospheric Structure Beneath Jeju Volcanic Island by Teleseismic Traveltime Tomography. J. Geophys. Res. Solid Earth 123, 6784–6801. https://doi.org/10.1029/2018JB015979

Staudacher, T., Allègre, C.J., 1988. Recycling of oceanic crust and sediments: the noble gas subduction barrier. Earth Planet. Sci. Lett. 89, 173–183. https://doi.org/10.1016/0012-821X(88)90170-7

Straub, S.M., LaGatta, A.B., Martin-Del Pozzo, A.L., Langmuir, C.H., 2008. Evidence from high-Ni olivines for a hybridized peridotite/pyroxenite source for orogenic andesites from the central Mexican Volcanic Belt. Geochemistry, Geophys. Geosystems 9, n/a-n/a. https://doi.org/10.1029/2007GC001583

Stuart, F.M., Lass-Evans, S., Fitton, J.G., Ellam, R.M., 2003. High $^{3}He/^{4}He$ ratios in picritic basalts from Baffin Island and the role of a mixed reservoir in mantle plumes. Nature 424, 57–59. https://doi.org/10.1038/nature01711

Su, F., Xiao, Y., He, H., Su, B., Wang, Y., Zhu, R., 2014. He and Ar isotope geochemistry of pyroxene megacrysts and mantle xenoliths in Cenozoic basalt from the Changle-Linqu area in western Shandong. Chinese Sci. Bull. 59, 396–411. https://doi.org/10.1007/s11434-013-0027-2

Sumino, H., Nakai, S.N.I., Nagao, K., Notsu, K., 2000. High 3He/4He ratio in xenoliths from Takashima: Evidence for plume type volcanism in southwestern Japan. Geophys. Res. Lett. 27, 1211–1214. https://doi.org/10.1029/1999GL008438

Sun, S. -s., McDonough, W.F., 1989. Chemical and isotopic systematics of oceanic basalts: implications for mantle composition and processes. Geol. Soc. London, Spec. Publ. 42, 313

LP – 345. https://doi.org/10.1144/GSL.SP.1989.042.01.19

Tang, H., Matsumoto, T., Zheng, J., Czuppon, G., Yu, C., Miyakawa, C., Ping, X., 2014. Heterogeneous lithospheric mantle metasomatism in the eastern North China Craton: He-Ar isotopes in peridotite xenoliths from Cenozoic basalts. J. Asian Earth Sci. 80, 185–196. https://doi.org/10.1016/j.jseaes.2013.11.012

Tao, K., Grand, S.P., Niu, F., 2018. Seismic Structure of the Upper Mantle Beneath Eastern Asia From Full Waveform Seismic Tomography. Geochemistry, Geophys. Geosystems 19, 2732–2763. https://doi.org/10.1029/2018GC007460

Tatsumi, Y., Shukuno, H., Yoshikawa, M., Chang, Q., Sato, K., Lee, M.W., 2005. The petrology and geochemistry of volcanic rocks on Jeju Island: Plume magmatism along the Asian continental margin. J. Petrol. 46, 523–553. https://doi.org/10.1093/petrology/egh087

Walter, M., 1998. Melting of Garnet Peridotite and the Origin of Komatiite and Depleted Lithosphere. J. Petrol. 39, 29–60. https://doi.org/10.1093/petrology/39.1.29

Wei, W., Zhao, D., Xu, J., Wei, F., Liu, G., 2015. P and S wave tomography and anisotropy in Northwest Pacific and East Asia: Constraints on stagnant slab and intraplate volcanism. J. Geophys. Res. Solid Earth 120, 1642–1666. https://doi.org/10.1002/2014JB011254

Williams, A.J., Stuart, F.M., Day, S.J., Phillips, W.M., 2005. Using pyroxene microphenocrysts to determine cosmogenic ^{3}He concentrations in old volcanic rocks: An example of landscape development in central Gran Canaria. Quat. Sci. Rev. 24, 211–222. https://doi.org/10.1016/j.quascirev.2004.07.004

Woo, Y., Yang, K., Kil, Y., Yun, S.H., Arai, S., 2014. Silica- and LREE-enriched spinel peridotite xenoliths from the Quaternary intraplate alkali basalt, Jeju Island, South Korea: Old subarc fragments? Lithos 208, 312–323. https://doi.org/10.1016/j.lithos.2014.09.003

Xia, B., Thybo, H., Artemieva, I.M., 2020. Lithosphere Mantle Density of the North China Craton. J. Geophys. Res. Solid Earth 125, 1–23. https://doi.org/10.1029/2020JB020296

Xu, Y., 2002. Evidence for crustal components in the mantle and constraints on crustal recycling mechanisms: Pyroxenite xenoliths from Hannuoba, North China. Chem. Geol. 182, 301–322. https://doi.org/10.1016/S0009-2541(01)00300-X

Xu, Y.G., Sun, M., Yan, W., Liu, Y., Huang, X.L., Chen, X.M., 2002. Xenolith evidence for polybaric melting and stratification of the upper mantle beneath South China. J. Asian Earth Sci. 20, 937–954. https://doi.org/10.1016/S1367-9120(01)00087-6

Xu, Z., Zheng, Y.-F., He, H.-Y., Zhao, Z.-F., 2014. Phenocryst He–Ar isotopic and whole-rock geochemical constraints on the origin of crustal components in the mantle source of Cenozoic continental basalt in eastern China. J. Volcanol. Geotherm. Res. 272, 99–110. https://doi.org/10.1016/j.jvolgeores.2014.01.001

Xu, Z., Zheng, Y.F., Zhao, Z.F., 2017. The origin of Cenozoic continental basalts in east-central China: Constrained by linking Pb isotopes to other geochemical variables. Lithos 268–271, 302–319. https://doi.org/10.1016/j.lithos.2016.11.006

Yamamoto, J., Kaneoka, I., Nakai, S., Kagi, H., Prikhod'ko, V.S., Arai, S., 2004. Evidence for subduction-related components in the subcontinental mantle from low 3He/4He and 40Ar/36Ar ratio in mantle xenoliths from Far Eastern Russia. Chem. Geol. 207, 237–259. https://doi.org/10.1016/j.chemgeo.2004.03.007

Yang, K., Arai, S., Yu, J. eun, Yun, S.H., Kim, J.S., Hwang, J.Y., 2012a. Gabbroic xenoliths and megacrysts in the Pleisto-Holocene alkali basalts from Jeju Island, South Korea: The implications for metasomatism of the lower continental crust. Lithos 142–143, 201–215. https://doi.org/10.1016/j.lithos.2012.03.006

Yang, K., Szabó, C., Arai, S., Yu, J.E., Jung, H., 2012b. Silica enrichment of Group II xenoliths by evolved alkali basalt from Jeju Island, South Korea: Implication for modification of intraplate deep-seated rocks. Mineral. Petrol. 106, 107–130. https://doi.org/10.1007/s00710-012-0222-x

Yang, Z.F., Li, J., Liang, W.F., Luo, Z.H., 2016. On the chemical markers of pyroxenite contributions in continental basalts in Eastern China: Implications for source lithology and the origin of basalts. Earth-Science Rev. 157, 18–31. https://doi.org/10.1016/j.earscirev.2016.04.001

Yoo, H.J., Herrmann, R.B., Cho, K.H., Lee, K., 2007. Imaging the three-dimensional crust of the Korean Peninsula by joint inversion of surface-wave dispersion and teleseismic receiver functions. Bull. Seismol. Soc. Am. 97, 1002–1011. https://doi.org/10.1785/0120060134

Yu, S.-Y., Xu, Y.-G., Ma, J.-L., Zheng, Y.-F., Kuang, Y.-S., Hong, L.-B., Ge, W.-C., Tong, L.-X., 2010. Remnants of oceanic lower crust in the subcontinental lithospheric mantle: Trace element and Sr–Nd–O isotope evidence from aluminous garnet pyroxenite xenoliths from Jiaohe, Northeast China. Earth Planet. Sci. Lett. 297, 413–422. https://doi.org/10.1016/j.epsl.2010.06.043

Yu, Z., Zhai, S., Guo, K., Zhou, Y., Zong, T., 2016. Helium isotopes in volcanic rocks from the Okinawa Trough-impact of volatile recycling and crustal contamination. Geol. J. 51, 376–386. https://doi.org/10.1002/gj.2794

Zhao, D., Tian, Y., Lei, J., Liu, L., Zheng, S., 2009. Seismic image and origin of the Changbai intraplate volcano in East Asia: Role of big mantle wedge above the stagnant Pacific slab. Phys. Earth Planet. Inter. 173, 197–206. https://doi.org/10.1016/j.pepi.2008.11.009

Table 1. Major and trace element compositions of the Jeju basalts

Sample	DB-01	DB-02	DB-03	SB-01	KB-01
Major elements (wt%) by XRF					
SiO_2	49.75	49.88	50.01	51.96	51.99
Al_2O_3	16.00	15.68	15.72	14.65	14.86
TiO_2	2.96	2.90	2.94	2.41	2.09
Fe_2O_3	12.74	12.83	12.87	12.39	12.27
MnO	0.15	0.15	0.15	0.15	0.15
MgO	5.07	5.30	5.20	5.58	5.59
CaO	8.53	8.38	8.43	9.09	9.44
Na_2O	2.82	2.96	2.92	2.36	2.36
K_2O	1.37	1.45	1.45	0.67	0.61
P_2O_5	0.63	0.59	0.60	0.37	0.30
LOI	-0.18	-0.26	-0.41	0.20	0.20
Total	99.85	99.86	99.88	99.84	99.86
Trace elements (ppm) by LA-ICP-MS					
Sc	16.94	16.99	17.20	21.49	21.96
V	165.82	165.05	166.77	164.27	162.67
Cr	112.17	121.85	118.17	190.80	190.57
Mn	891.15	912.37	905.18	957.92	946.47
Co	140.53	120.09	144.42	182.12	162.94
Ni	78.18	74.21	81.22	84.09	76.20
Zn	105.61	112.83	106.72	110.74	109.08
Ga	18.81	18.63	18.21	18.37	18.36
Rb	20.94	25.38	24.93	12.68	13.44
Sr	499.41	487.00	491.00	318.13	298.49
Y	18.55	17.65	18.02	19.90	19.41
Zr	182.73	176.72	176.49	139.24	116.01
Nb	34.11	32.35	32.48	16.81	14.59
Mo	2.03	2.04	1.90	1.30	1.29
Cs	0.27	0.29	0.29	0.23	0.22
Ba	334.89	319.66	323.29	162.88	161.62
La	24.00	23.05	22.91	13.37	12.40
Ce	47.77	45.97	45.96	28.83	25.58
Pr	5.78	5.44	5.52	3.85	3.35
Nd	24.60	22.86	23.27	17.54	15.41
Sm	5.47	5.44	5.31	4.51	4.30
Eu	1.82	1.83	1.85	1.67	1.56
Gd	5.18	5.11	4.98	5.12	4.85
Tb	0.72	0.67	0.68	0.76	0.66

Dy	4.16	3.99	3.92	4.26	4.13
Ho	0.70	0.69	0.68	0.79	0.79
Er	1.77	1.80	1.65	1.99	1.90
Tm	0.22	0.23	0.23	0.25	0.26
Yb	1.48	1.35	1.35	1.56	1.49
Lu	0.19	0.20	0.21	0.22	0.21
Hf	4.53	4.09	4.31	3.74	3.15
Ta	2.17	2.06	2.07	1.15	1.00
Pb	2.65	2.61	2.78	2.14	2.33
Th	4.01	3.67	3.89	2.06	2.13
U	0.87	0.78	0.83	0.46	0.54

Table 2. Representative major element compositions of the Jeju xenoliths

sample	**SX-01**								**SX-02**						**SX-03**					
mineral	Olivine (n=3)		Clinopyroxene (n=3)		Orthopyroxene (n=3)		Spinel (n=3)		Olivine (n=3)		Clinopyroxene (n=3)		Orthopyroxene (n=3)		Olivine (n=4)		Clinopyroxene (n=3)		Orthopyroxene (n=3)	
(wt%)	Mean	RSD%	Mean	RSD%	Mean	RSD%	Mean	RSD%	Mean	RSD%	Mean	RSD%	Mean	RSD%	Mean	RSD%	Mean	RSD%	Mean	RSD%
SiO2	41.27	0.3	51.86	0.5	55.09	0.2	0.04	12.5	40.32	0.1	51.72	0.2	54.84	0.1	40.25	0.2	51.93	0.2	54.93	0.5
TiO2	0.01	94.5	0.47	3.6	0.12	5.5	0.11	3.9	0.01	42.0	0.52	0.9	0.13	15.1	0.01	110.4	0.35	0.8	0.09	19.1
Al2O3	0.02	9.1	6.62	2.4	4.53	3.9	58.30	0.1	0.02	68.7	6.17	1.0	3.98	2.5	0.01	37.8	6.59	2.3	4.35	7.6
FeO	9.60	1.4	2.79	5.9	6.40	13.2	11.16	1.2	11.03	0.9	3.12	3.9	6.55	3.2	10.95	5.4	2.81	1.7	6.31	0.4
MnO	0.12	1.8	0.09	19.0	0.11	16.9	0.12	1.4	0.14	7.4	0.06	50.4	0.14	21.6	0.15	2.6	0.08	11.6	0.12	15.0
MgO	49.31	0.1	15.63	0.8	33.23	1.2	20.50	0.2	47.98	0.1	15.44	0.8	33.44	0.3	48.01	0.8	15.51	0.5	33.56	0.4
CaO	0.05	6.2	20.94	0.2	0.66	3.7	0.00		0.06	9.7	20.15	0.4	0.65	7.2	0.06	11.3	20.70	0.2	0.66	6.2
K2O	0.00	77.6	0.01	76.6	0.01	95.4	0.00	141.4	0.00	141.4	0.00	141.4	0.00	141.4	0.00	100.0	0.00		0.01	88.2
Na2O	0.01	141.4	1.32	2.8	0.07	9.5	0.01	75.0	0.02	58.7	1.61	2.8	0.09	9.2	0.02	68.8	1.47	1.2	0.08	11.3
Cr2O3	0.00	141.4	0.74	3.9	0.35	9.6	9.08	0.9	0.01	100.9	1.26	1.4	0.47	13.6	0.01	149.6	0.96	4.1	0.40	13.1
Total	100.40	0.1	100.47	0.3	100.55	0.3	99.32	0.1	99.59	0.1	100.06	0.3	100.30	0.2	99.47	0.1	100.40	0.1	100.51	0.0
Mg#	90.15	0.1	90.88	0.6	90.26	1.4	76.60	0.3	88.57	0.1	89.81	0.5	90.09	0.3	88.66	0.7	90.79	0.1	90.46	0.1
Cr#							9.46	0.7												

Table 2. Continued

sample	SX-04						SX-05						SX-06							
mineral	Olivine (n=4)		Clinopyroxene (n=3)		Orthopyroxene (n=4)		Olivine (n=3)		Clinopyroxene (n=4)		Orthopyroxene (n=3)		Olivine (n=3)		Clinopyroxene (n=3)		Orthopyroxene (n=3)		Spinel (n=4)	
(wt%)	Mean	RSD%	Mean	RSD%	Mean	RSD%	Mean	RSD%	Mean	RSD%	Mean	RSD%	Mean	RSD%	Mean	RSD%	Mean	RSD%	Mean	RSD%
SiO2	40.69	0.1	52.15	0.2	54.94	0.4	40.96	0.1	52.25	0.4	54.84	0.3	40.60	0.4	51.95	0.1	54.92	0.7	0.04	13.1
TiO2	0.01	105.1	0.42	8.2	0.11	14.8	0.00	0.0	0.45	3.3	0.11	9.9	0.00	114.7	0.51	5.5	0.13	12.7	0.13	7.2
Al2O3	0.01	32.2	5.97	1.1	4.15	6.1	0.01	41.6	6.69	1.4	4.57	3.4	0.02	36.2	6.74	0.5	4.70	7.8	58.65	0.5
FeO	10.38	1.8	2.66	2.5	6.53	1.5	10.31	1.8	2.84	3.5	6.40	1.9	10.47	0.9	3.01	3.8	6.51	2.0	11.32	3.1
MnO	0.11	17.6	0.09	13.4	0.12	17.5	0.14	12.8	0.07	11.0	0.12	5.6	0.12	15.2	0.08	4.7	0.12	24.3	0.11	14.1
MgO	48.26	0.1	15.40	0.7	33.53	0.5	48.62	0.5	15.74	0.5	33.49	0.2	48.55	0.4	15.55	1.0	33.41	0.4	20.65	0.3
CaO	0.06	6.9	20.94	0.8	0.60	9.5	0.06	3.6	20.52	0.5	0.70	3.8	0.06	4.9	20.41	0.4	0.67	6.5	0.00	173.2
K2O	0.00	102.5	0.01	72.8	0.00	153.8	0.00	141.4	0.00		0.00	76.0	0.00	59.3	0.01	75.9	0.01	20.9	0.00	100.9
Na2O	0.00	173.2	1.47	2.7	0.08	17.4	0.00	141.4	1.44	2.6	0.10	11.7	0.01	97.8	1.53	1.9	0.08	5.9	0.00	173.2
Cr2O3	0.01	65.7	1.07	2.7	0.51	10.0	0.01	101.8	0.81	7.7	0.39	6.3	0.01	141.4	0.73	3.4	0.34	14.3	8.89	2.5
Total	99.52	0.2	100.18	0.2	100.57	0.2	100.12	0.0	100.80	0.2	100.72	0.1	99.83	0.2	100.52	0.2	100.89	0.3	99.79	0.3
Mg#	89.23	0.2	91.16	0.2	90.16	0.2	89.36	0.2	90.81	0.3	90.31	0.2	89.21	0.1	90.21	0.4	90.15	0.2	76.48	0.8
Cr#																			9.23	2.6

Table 3. Major and trace element compositions of olivine phenocrysts in the Jeju basalts

sample	**DB-01**				**DB-02**					**DB-03**					
Type	Olivine phenocryst in basalts														
Grain	ol-1	ol-2	ol-3	ol-4	ol-5	ol-1	ol-2	ol-3	ol-4	ol-5	ol-1	ol-2c	ol-2r	ol-3	ol-4
Major element (wt%) by EPMA															
SiO_2	37.80	38.50	38.25	38.66	38.65	38.37	38.56	38.40	38.06	38.50	38.22	37.88	38.72	38.07	38.28
TiO_2	0.04	0.02	0.00	0.02	0.02	0.02	0.03	0.01	0.01	0.02	0.03	0.04	0.03	0.01	0.04
Al_2O_3	0.03	0.03	0.06	0.05	0.05	0.02	0.04	0.05	0.04	0.05	0.03	0.04	0.04	0.02	0.02
FeO	27.12	22.17	23.07	22.22	21.96	22.98	21.71	22.06	23.00	22.34	21.96	23.81	20.75	23.98	22.60
MnO	0.34	0.26	0.25	0.26	0.25	0.21	0.20	0.28	0.21	0.21	0.19	0.23	0.18	0.26	0.28
MgO	34.85	39.13	38.57	39.07	39.42	38.58	39.64	39.46	38.19	39.07	38.60	37.84	40.50	37.89	38.84
CaO	0.16	0.17	0.17	0.17	0.15	0.15	0.16	0.17	0.16	0.16	0.17	0.16	0.18	0.14	0.16
K_2O	0.00	0.01	0.00	0.00	0.00	0.00	0.00	0.00	0.01	0.00	0.01	0.02	0.02	0.00	0.02
Na_2O	0.00	0.01	0.00	0.02	0.00	0.02	0.00	0.02	0.00	0.01	0.02	0.05	0.02	0.02	0.04
Cr_2O_3	0.00	0.00	0.00	0.00	0.00	0.00	0.02	0.00	0.00	0.00	0.01	0.02	0.03	0.00	0.00
Total	100.33	100.29	100.36	100.47	100.51	100.36	100.37	100.46	99.68	100.36	99.23	100.08	100.47	100.39	100.28
Mg#	69.61	75.88	74.87	75.81	76.19	74.95	76.49	76.13	74.74	75.71	75.81	73.91	77.67	73.79	75.39
Trace element (ppm) by LA-ICP-MS															
Li	2.31	1.84	2.04	1.96		1.56	2.28	1.66	1.92	2.14	2.09	2.08		2.01	
Sc	5.38	5.04	4.91	4.83		6.96	7.39	6.90	6.25	6.82	5.40	4.95		5.69	
V	7.07	6.63	6.80	6.66		7.29	7.59	7.29	6.58	8.75	6.84	7.24		7.15	
Cr	LOD	33	30	29		25	53	36	22	22	25	31		14	
Co	207	204	206	217		228	211	215	228	201	222	228		214	
Ni	345	1308	1195	1315		1329	1677	1346	1210	1234	1292	1374		923	
Ga	0.18	0.18	0.17	0.19		0.20	0.23	0.24	0.18	0.25	0.20	0.15		0.22	

Table 3: Continued

sample	SB-01					KB-01					
Type	Olivine phenocryst in basalts										
Grain	ol-1	ol-2	ol-3	ol-4	ol-5	ol-1	ol-2	ol-3c	ol-3r	ol-4	ol-5
Major element (wt%) by EPMA											
SiO_2	39.10	39.13	39.03	39.13	39.06	39.21	38.98	38.65	38.52	39.07	38.91
TiO_2	0.01	0.02	0.01	0.02	0.00	0.02	0.00	0.03	0.00	0.01	0.00
Al_2O_3	0.03	0.03	0.02	0.03	0.05	0.01	0.05	0.03	0.02	0.02	0.04
FeO	19.90	18.87	18.93	18.93	18.85	18.79	19.79	20.32	21.61	19.08	19.45
MnO	0.18	0.21	0.23	0.23	0.21	0.21	0.22	0.24	0.27	0.19	0.19
MgO	40.96	41.72	41.67	41.69	41.71	41.29	41.10	40.51	39.72	41.39	41.20
CaO	0.20	0.21	0.20	0.20	0.19	0.21	0.20	0.22	0.20	0.21	0.23
K_2O	0.01	0.00	0.00	0.01	0.00	0.00	0.01	0.00	0.00	0.00	0.00
Na_2O	0.00	0.00	0.02	0.00	0.00	0.00	0.02	0.01	0.00	0.00	0.04
Cr_2O_3	0.03	0.04	0.05	0.05	0.04	0.05	0.03	0.05	0.03	0.02	0.04
Total	100.42	100.23	100.17	100.29	100.11	99.80	100.39	100.05	100.38	99.99	100.09
Mg#	78.58	79.76	79.69	79.69	79.77	79.66	78.73	78.04	76.61	79.45	79.06
Trace element (ppm) by LA-ICP-MS											
Li	1.99	1.71	1.73	1.91		1.95	1.86	1.91		1.60	
Sc	5.84	5.66	5.58	5.83		5.43	5.68	6.02		5.46	
V	7.33	5.95	5.95	6.77		6.41	7.04	7.21		6.54	
Cr	238	236	226	237		176	188	216		179	
Co	183	185	187	188		187	194	190		190	
Ni	1972	2008	1966	1977		1967	1980	1628		2029	
Ga	0.19	0.21	0.15	0.20		0.12	0.19	0.18		0.20	

Table 2. Major and trace element compositions of clinopyroxenes in the Jeju xenoliths

Sample	SX-01			SX-02			SX-03			SX-04			SX-05				SX-06		
Grain	cpx-4	cpx-5	cpx-6	cpx-1	cpx-2	cpx-3	cpx-1	cpx-2	cpx-3	cpx-1	cpx-2	cpx-3	cpx-1	cpx-2	cpx-3	cpx-4	cpx-1	cpx-2	cpx-3
Major element (wt%) by EPMA																			
SiO_2	51.7	52.2	51.7	51.6	51.8	51.8	52.0	51.8	52.0	52.0	52.3	52.2	52.5	52.1	52.4	52.0	52.0	52.0	51.9
TiO_2	0.5	0.5	0.4	0.5	0.5	0.5	0.4	0.4	0.4	0.4	0.4	0.5	0.5	0.5	0.4	0.4	0.5	0.6	0.5
Al_2O_3	6.4	6.6	6.8	6.2	6.1	6.2	6.4	6.8	6.6	6.1	5.9	5.9	6.8	6.6	6.6	6.7	6.8	6.7	6.8
FeO	2.6	2.8	3.0	3.1	3.0	3.3	2.8	2.8	2.7	2.6	2.8	2.7	2.9	3.0	2.7	2.8	3.1	3.1	2.9
MnO	0.1	0.1	0.1	0.1	0.0	0.1	0.1	0.1	0.1	0.1	0.1	0.1	0.1	0.1	0.1	0.1	0.1	0.1	0.1
MgO	15.8	15.7	15.5	15.4	15.6	15.3	15.6	15.5	15.5	15.3	15.5	15.4	15.8	15.8	15.7	15.6	15.8	15.4	15.5
CaO	20.9	20.9	21.0	20.0	20.2	20.2	20.6	20.7	20.7	20.9	20.8	21.2	20.6	20.3	20.6	20.6	20.4	20.5	20.3
K_2O	0.0	0.0	0.0	0.0	0.0	0.0	0.0	0.0	0.0	0.0	0.0	0.0	0.0	0.0	0.0	0.0	0.0	0.0	0.0
Na_2O	1.34	1.35	1.27	1.55	1.66	1.61	1.45	1.49	1.48	1.49	1.50	1.41	1.50	1.42	1.40	1.43	1.49	1.53	1.56
Cr_2O_3	0.7	0.8	0.8	1.3	1.2	1.3	0.9	1.0	1.0	1.1	1.0	1.1	0.7	0.8	0.9	0.9	0.7	0.8	0.7
Total	100.0	100.8	100.6	99.7	100.1	100.4	100.3	100.5	100.4	99.9	100.2	100.4	101.2	100.7	100.8	100.6	100.8	100.6	100.2
Mg#	91.5	91.0	90.1	89.8	90.3	89.3	90.7	90.7	91.0	91.3	91.0	91.2	90.8	90.5	91.2	90.7	90.1	89.9	90.7
Trace element (ppm) by LA-ICP-MS																			
Li	1.61	1.68	1.66	1.58	1.34	2.26	1.51	1.67	1.65	1.75	1.55	1.99	1.44	1.43	1.52	1.71	1.41	1.10	1.38
Sc	55.9	59.5	60.9	74.3	72.1	71.0	57.5	55.3	57.1	58.5	56.7	65.4	63.8	66.1	63.6	62.8	64.4	69.6	63.3
Ti	3023	3239	3159	3439	3076	3464	2210	2166	2325	2746	2641	2933	2892	2849	2903	2900	3341	3465	3348
V	272	287	284	279	263	271	261	256	264	253	248	259	272	275	270	271	279	289	279
Cr	4774	5093	5050	8520	6949	8838	6455	6754	6827	7951	8294	7389	6095	6086	5881	5953	4954	5069	5394
Mn	633	636	684	687	684	727	687	651	664	634	646	580	650	674	660	629	657	667	661
Co	20.8	21.1	21.6	22.0	22.2	22.8	21.4	20.7	20.7	20.0	20.2	20.1	21.6	22.3	21.9	21.2	22.0	22.0	21.0
Ni	339	348	349	367	362	363	335	332	334	321	329	341	339	341	330	326	340	340	326
Zn	13.2	10.5	18.1	13.3	12.4	14.9	10.5	10.6	10.9	9.8	12.5	10.3	11.2	15.8	10.7	10.2	10.4	12.6	10.8
Ga	3.52	3.60	3.64	4.24	3.85	4.64	4.01	3.46	3.63	3.68	4.14	3.52	3.88	3.73	3.62	3.68	4.19	4.20	4.26

Rb	LOD	LOD	LOD	LOD	LOD	LOD	LOD	LOD	LOD	LOD	LOD	LOD	LOD	LOD	LOD	LOD	LOD	LOD	LOD
Sr	6.6	6.3	13.2	99.7	75.0	118.6	40.0	19.4	18.3	32.1	31.8	31.3	15.4	18.2	31.1	15.6	25.2	51.9	40.1
Y	17.5	18.1	17.8	16.6	15.2	16.4	15.5	15.2	15.7	12.2	12.0	12.1	17.7	17.7	18.0	18.2	18.9	18.4	18.5
Zr	7.3	7.7	7.7	84.2	67.8	83.4	10.7	10.3	10.1	12.1	11.5	11.6	13.8	14.1	19.5	14.0	9.8	11.2	9.7
Nb	0.17	0.03	0.46	0.31	0.15	0.32	0.52	0.19	0.16	0.02	0.01	0.01	0.09	0.18	0.28	0.12	0.18	0.38	0.26
Mo	LOD	LOD	LOD	0.02	0.01	0.05	LOD	LOD	LOD	LOD	LOD	LOD	LOD	LOD	LOD	LOD	LOD	LOD	LOD
Cs	LOD	LOD	LOD	LOD	LOD	LOD	LOD	LOD	LOD	0.01	LOD	LOD	LOD	LOD	LOD	LOD	LOD	LOD	LOD
Ba	LOD	LOD	LOD	0.03	0.01	LOD	LOD	LOD	0.07	0.07	0.08	LOD	LOD	LOD	LOD	0.00	0.06	LOD	LOD
La	0.20	0.03	1.52	6.25	3.89	7.94	3.57	0.75	0.46	0.20	0.19	0.18	0.18	0.67	2.38	0.31	0.54	2.90	1.88
Ce	0.51	0.32	2.60	14.41	6.38	18.02	4.73	1.17	0.99	1.04	1.02	0.96	0.84	1.53	4.20	0.86	1.67	5.62	3.86
Pr	0.15	0.19	0.33	1.78	0.75	2.11	0.49	0.26	0.23	0.23	0.23	0.23	0.29	0.28	0.52	0.29	0.37	0.72	0.51
Nd	1.71	1.77	2.17	7.55	4.19	8.73	2.30	1.99	1.95	1.98	1.88	2.04	2.23	2.29	2.91	2.26	2.73	3.68	3.08
Sm	1.19	1.22	1.14	2.21	1.45	2.31	1.00	1.06	1.05	1.16	1.00	1.12	1.15	1.31	1.34	1.34	1.19	1.60	1.32
Eu	0.47	0.52	0.48	0.80	0.63	0.87	0.52	0.45	0.45	0.44	0.46	0.47	0.57	0.53	0.51	0.54	0.62	0.64	0.59
Gd	2.23	1.96	2.07	2.42	1.96	2.75	1.80	1.81	1.82	1.71	1.79	1.88	2.27	2.12	2.24	2.18	2.18	2.43	2.17
Tb	0.42	0.42	0.40	0.43	0.40	0.46	0.36	0.33	0.35	0.31	0.32	0.33	0.44	0.41	0.45	0.43	0.44	0.43	0.48
Dy	2.93	3.27	3.03	2.96	2.50	3.05	2.65	2.56	2.67	2.24	2.07	2.02	3.17	3.09	3.19	3.20	3.27	3.49	3.49
Ho	0.67	0.71	0.66	0.67	0.56	0.65	0.59	0.63	0.58	0.47	0.43	0.47	0.76	0.70	0.68	0.70	0.70	0.73	0.69
Er	1.93	1.95	2.01	1.82	1.71	1.81	1.79	1.76	1.77	1.42	1.40	1.32	2.02	1.97	2.18	2.23	2.20	2.17	2.15
Tm	0.28	0.28	0.27	0.24	0.24	0.24	0.25	0.23	0.26	0.19	0.20	0.20	0.30	0.27	0.30	0.28	0.29	0.30	0.31
Yb	1.83	2.03	1.92	1.57	1.59	1.62	1.56	1.64	1.72	1.24	1.16	1.22	1.91	1.87	1.84	1.94	2.18	2.06	2.09
Lu	0.24	0.27	0.27	0.23	0.22	0.21	0.23	0.24	0.21	0.21	0.20	0.19	0.28	0.25	0.28	0.30	0.28	0.29	0.28
Hf	0.52	0.53	0.55	2.52	2.21	2.52	0.53	0.40	0.44	0.51	0.53	0.55	0.65	0.65	0.64	0.65	0.56	0.55	0.56
Ta	LOD	LOD	0.01	0.02	LOD	0.01	0.02	LOD	LOD	0.00	LOD	LOD	LOD	LOD	0.04	LOD	0.02	0.02	0.01
Pb	0.06	0.03	0.06	0.31	0.35	0.32	0.31	0.23	0.25	LOD	LOD	LOD	0.05	0.05	0.11	0.07	0.09	0.13	0.17
Th	0.11	0.03	0.28	0.62	0.63	0.66	1.07	0.70	0.62	LOD	LOD	LOD	0.18	0.23	0.59	0.29	0.12	0.40	0.29
U	0.03	0.01	0.06	0.13	0.15	0.15	0.22	0.17	0.14	0.00	LOD	LOD	0.05	0.08	0.14	0.09	0.04	0.09	0.07

Table 3. Helium isotope compositions of the basalt and xenolith samples in Jeju Island

Sample	Location	Rock Type	Mineral	Mass (g)	Age (Ma)	R/Ra	d	d%	4He ccSTP/g	Error	3He ccSTP/g	Error
DB-01	Daepodong	Basalt	olivine	0.384	<0.1	7.3	0.4	6%	1.2E-08	6.3E-12	1.2E-13	7.4E-15
DB-02	Daepodong	Basalt	olivine	0.327	<0.1	6.8	0.3	5%	1.9E-08	1.0E-11	1.8E-13	1.1E-14
DB-03	Daepodong	Basalt	olivine	0.407	<0.1	5.9	0.6	9%	1.2E-08	1.4E-11	4.0E-13	2.5E-14
SB-01	Sinchang-ri	Basalt	olivine	0.47	<0.1	3.5	0.1	4%	8.2E-08	4.4E-11	4.0E-13	2.5E-14
KB-01	Kwideok-ri	Basalt	olivine	0.442	<0.1	6.9	0.3	4%	2.1E-08	1.1E-11	2.0E-13	1.3E-14
DB-02	Daepodong	Basalt	clinopyroxene	0.655	<0.1	5.6	0.2	4%	4.7E-08	2.5E-11	3.7E-13	2.3E-14
DB-03	Daepodong	Basalt	clinopyroxene	0.617	<0.1	6.4	0.2	3%	4.1E-08	2.2E-11	3.7E-13	2.3E-14
SX-01	Sinsan-ri	xenolith	olivine	0.552	<0.1	5.8	0.7	12%	1.5E-09	8.2E-12	1.3E-14	7.8E-16
SX-02	Sinsan-ri	xenolith	olivine	0.45	<0.1	6.5	0.3	5%	1.3E-08	7.2E-12	1.2E-13	7.5E-15
SX-03	Sinsan-ri	xenolith	olivine	0.479	<0.1	6.5	0.1	2%	1.8E-07	9.6E-11	1.6E-12	1.0E-13
SX-04	Sinsan-ri	xenolith	olivine	0.395	<0.1	6.2	0.7	11%	6.1E-09	3.3E-12	5.3E-14	1.3E-15
SX-05	Sinsan-ri	xenolith	olivine	0.444	<0.1	4.5	0.5	10%	5.3E-09	2.8E-12	3.4E-14	2.1E-15
SX-06	Sinsan-ri	xenolith	olivine	0.55	<0.1	2.9	0.2	7%	1.5E-08	8.0E-12	5.6E-14	3.5E-15

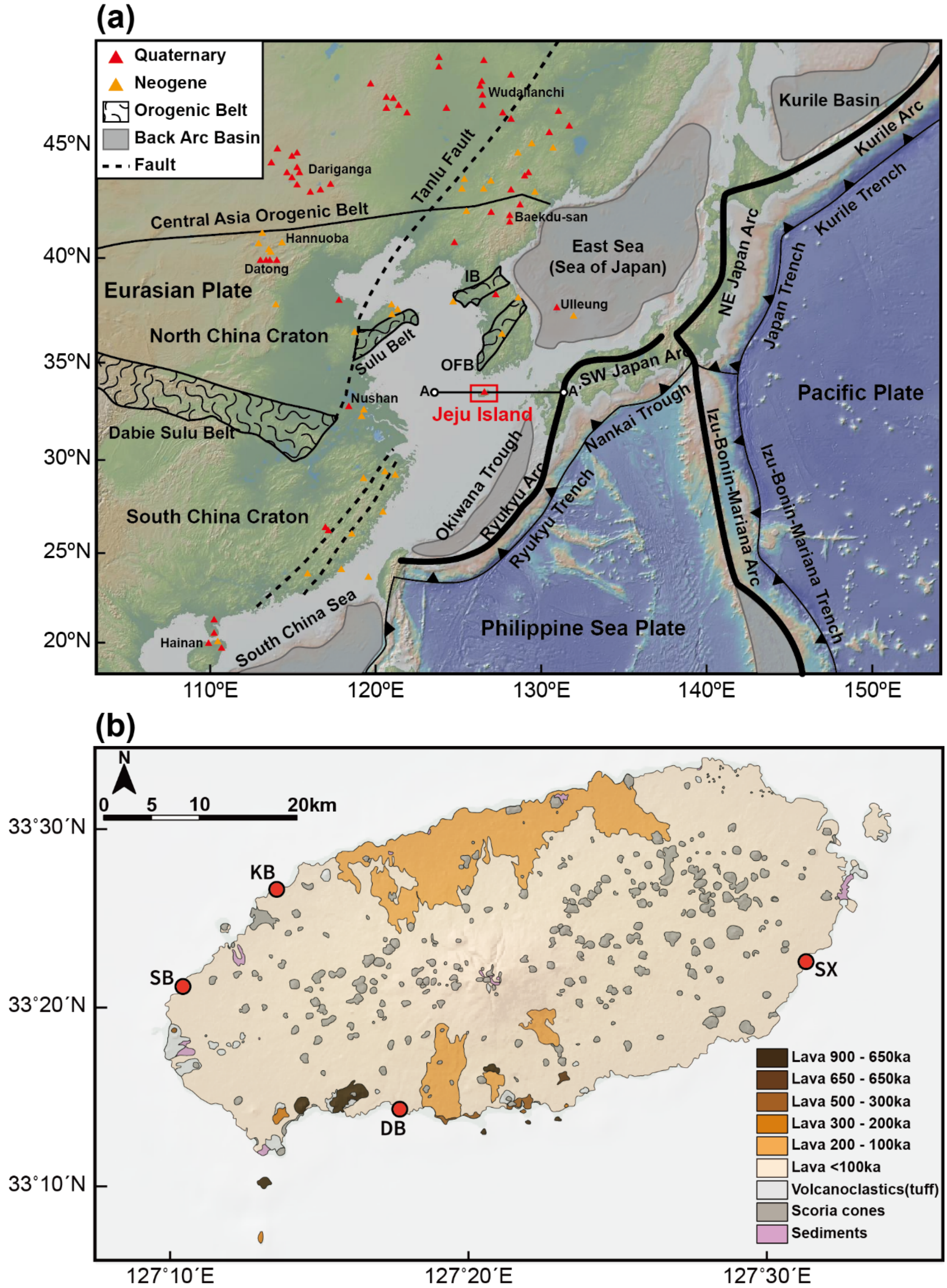

Fig. 1. (a) Geological map of East Asia with volcanic fields indicated by Choi et al. (2006), Chen et al. (2007), and Guo et al. (2014). Abbreviations in the diagram are IB (Imjingang Belt) and OFB (Okcheon Fold Belt). A-A' is the location of the vertical cross-section of mantle tomography (Fig. 9). (b) Geological map of Jeju Island (modified after Koh et al., 2013), and the sampling sites are shown. Abbreviations in the diagram are KB (Kwideok-Ri Basalt), SB (Sinchang-Ri Basalt), DB (Daepodong Basalt), and SX (Sinsan-Ri xenolith)

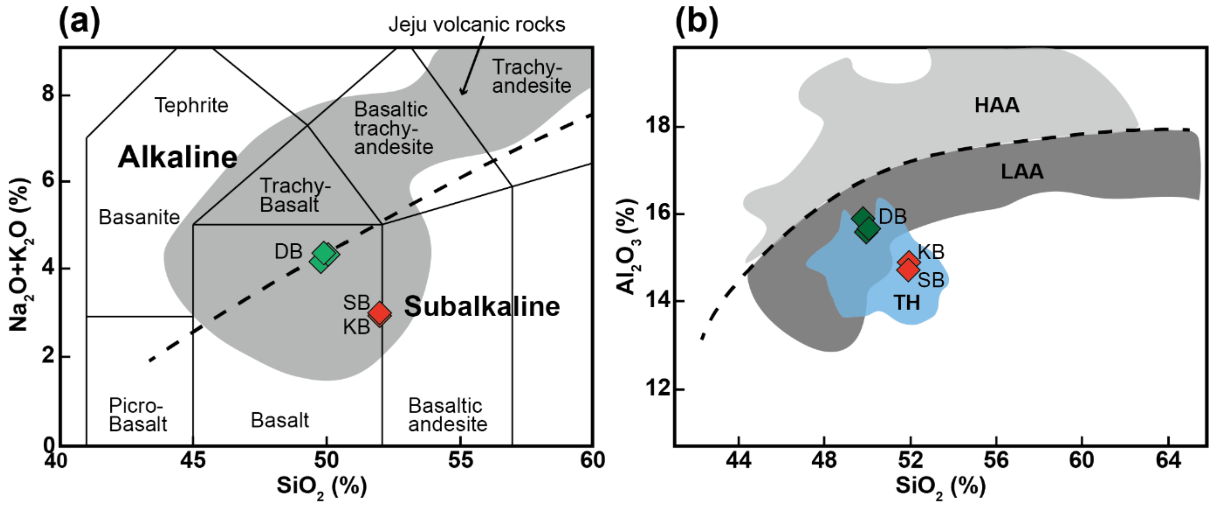

Fig. 2. Classification of the Jeju island basalt samples. (a) Total alkali (Na_2O + K_2O) versus SiO_2 diagram, and (b) Al_2O_3 vs. SiO_2 diagram. The data sources indicating the areas in (a) and (b) are from Baek et al. (2014) and references therein.

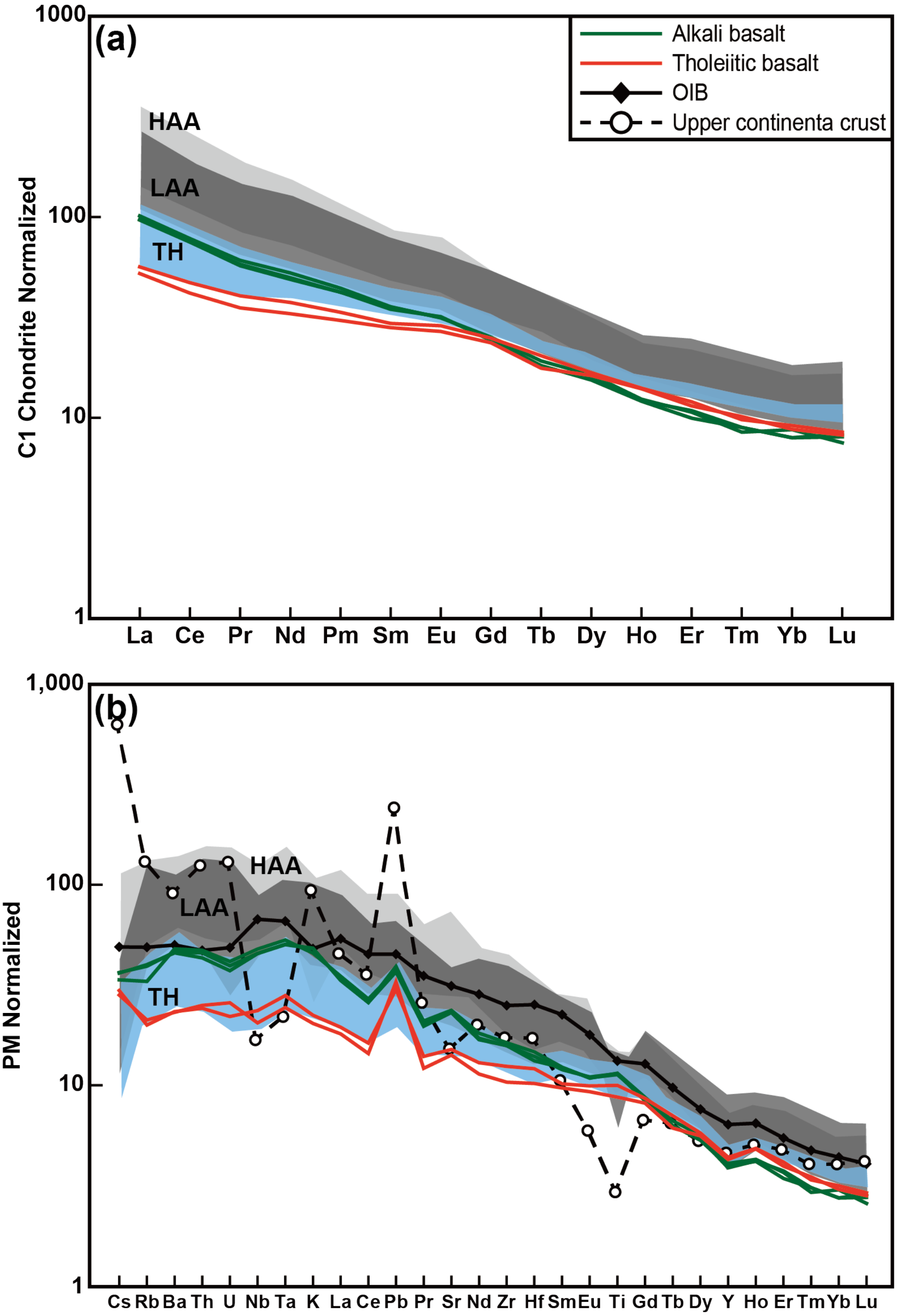

Fig. 3. Rare earth element (REE) and trace element patterns of the Jeju basalt samples (a) REE patterns normalized to the C1 chondrite values (Sun and McDonough, 1989). (b) Trace element patterns normalized to the primitive mantle (Sun and McDonough, 1989). The shaded areas indicate high-Al alkali (HAA), low-Al alkali (LAA), and tholeiite (TH) which are previously reported basalt samples ($SiO_2 < 52\%$, Kim et al., 2019). Typical ocean island basalt (OIB) and upper continental crust compositions are from Sun and McDonough (1989) and Rudnick and Gao (2003).

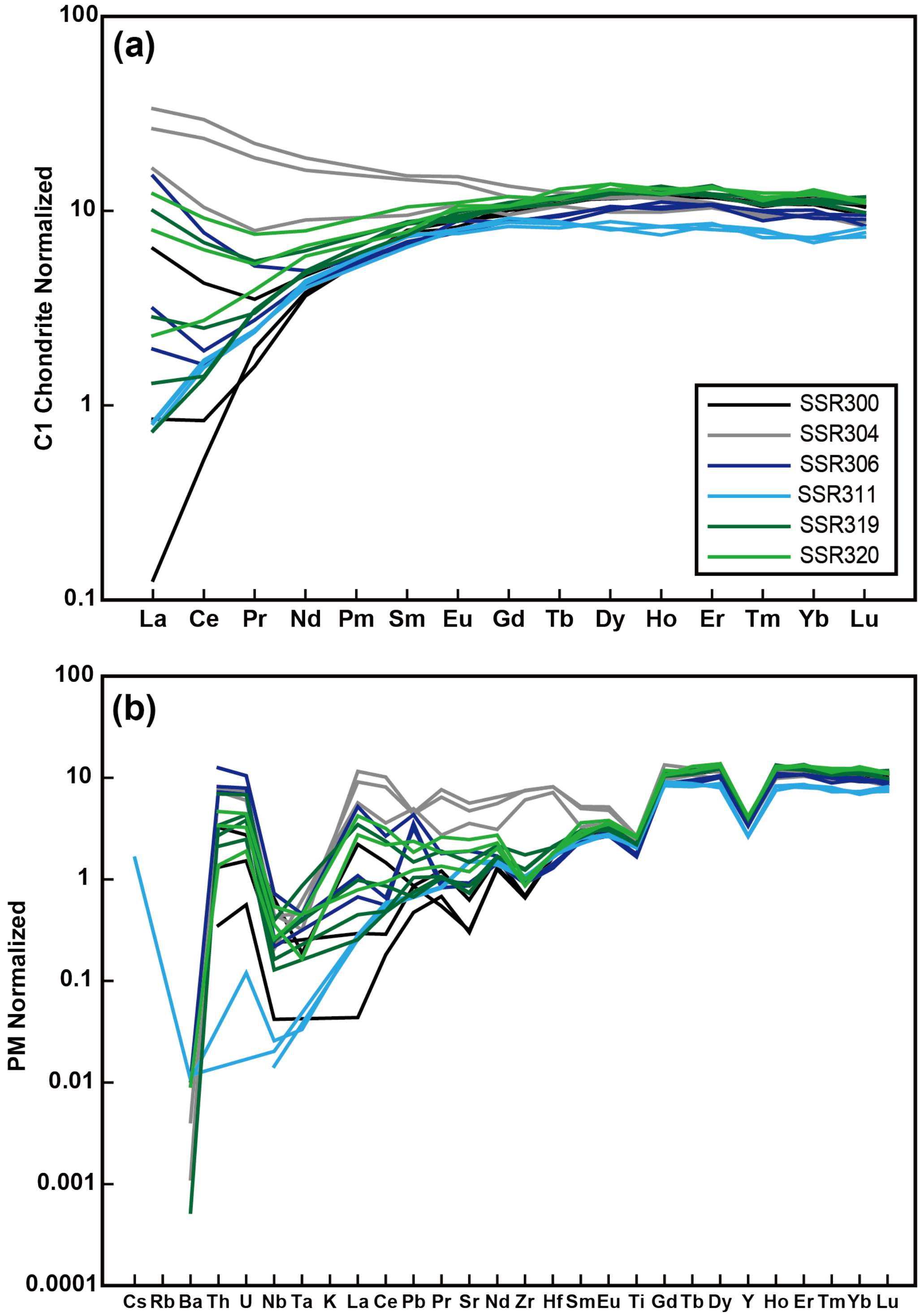

Fig. 4. Rare-earth-element (REE) and trace element patterns of clinopyroxenes in the Jeju xenolith samples (a) REE patterns normalized to the C1 chondrite values (Sun and McDonough, 1989). Various LREE enrichments with relatively flat MREE and HREE patterns are shown. (b) Trace element patterns normalized to the primitive mantle (Sun and McDonough, 1989). Nb-Ta depletion and U-Th enrichment are observed.

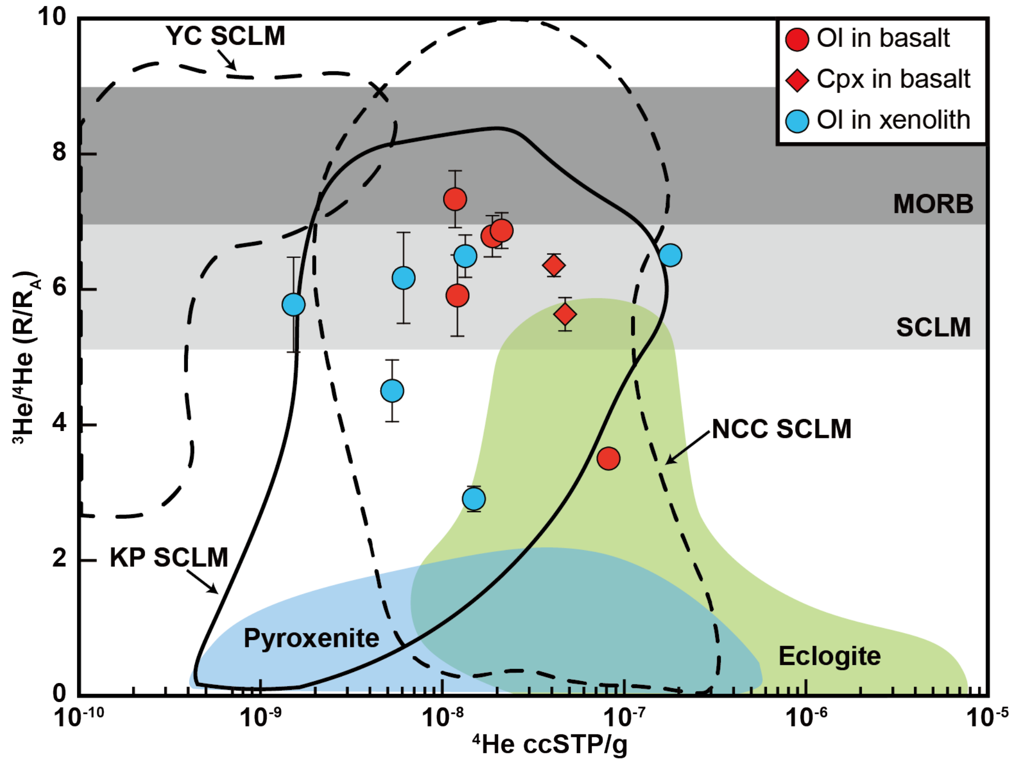

Fig. 5. $^{3}He/^{4}He$ ratios (R/Ra) vs. ^{4}He contents of the Jeju Island basalts and xenoliths. Reference data are from Graham (2002) for mid-ocean ridge basalt (MORB); Gautheron and Moreira (2002) for Subcontinental lithospheric mantle (SCLM); Kim et al. (2005) for Korean Peninsula (KP) SCLM; Correale et al. (2016) for Yangtze Craton (YC) SCLM; Tang et al. (2014) for North China Craton (NCC) SCLM; Day et al. (2015) for pyroxenite and eclogite, respectively.

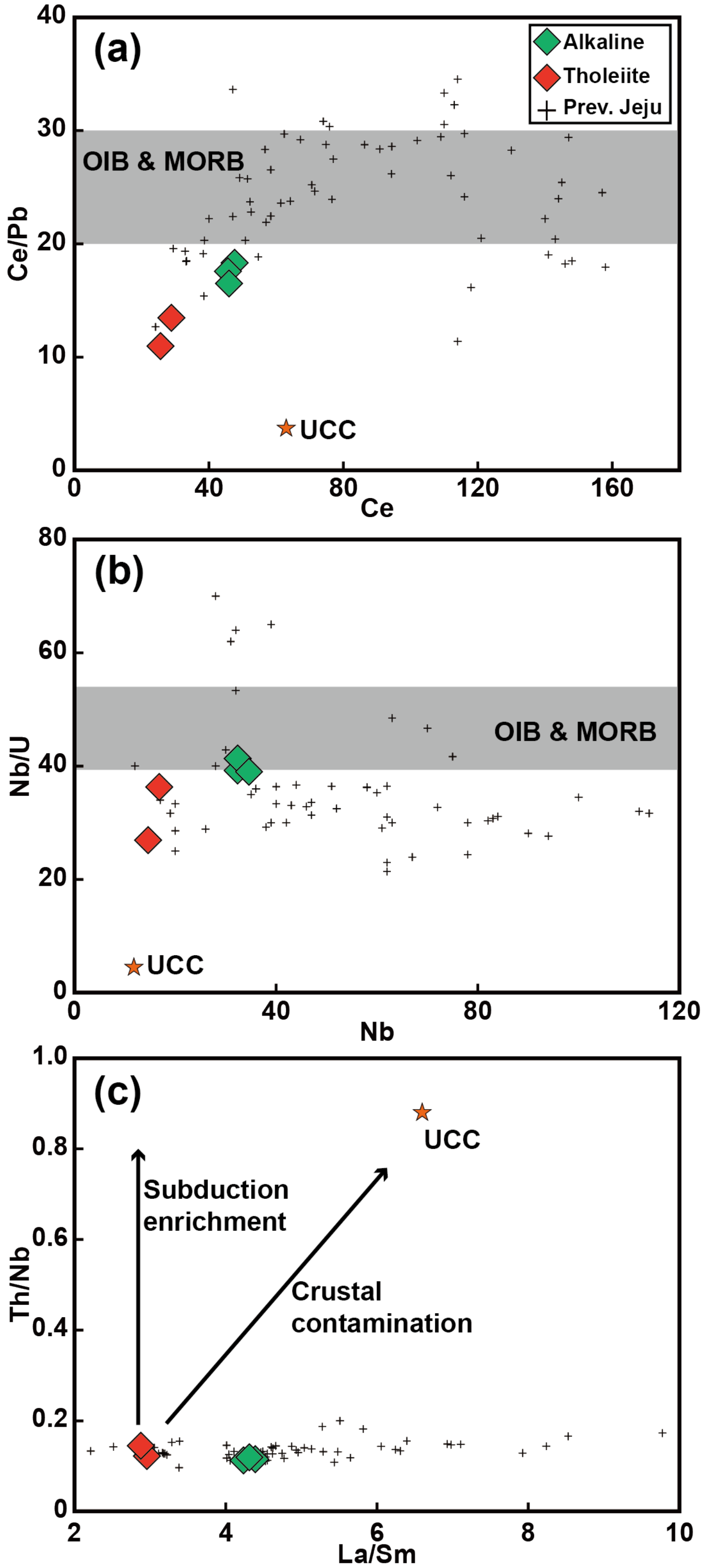

Fig. 6. Crustal assimilation indicators with (a) Ce/Pb vs. Ce (ppm), (b) Nb/U vs. Nb (ppm), and (c) Th/Nb vs. La/Sm. The cross dots indicate the previously reported Jeju basalt data (Kim et al., 2019) The orange star represents the upper continental crust (UCC) value (Rudnick and Gao, 2003). The shaded area means the OIB and MORB ranges (Ce/Pb: 20-30; Nb/U: 37-57; Hofmann et al., 1986)

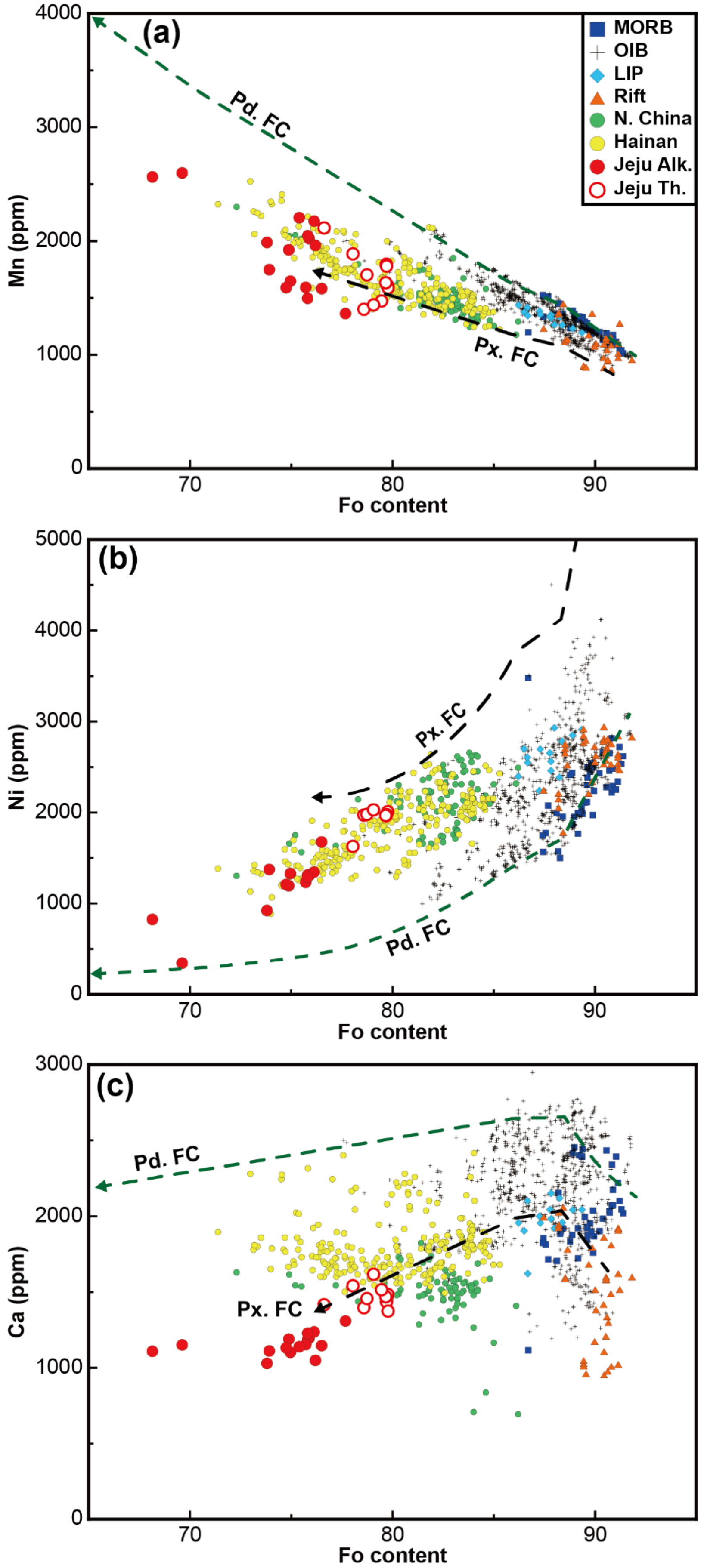

(a)
MORB
OIB
LIP
Rift
N. China
Hainan
Jeju Alk.
Jeju Th.
Pd. FC
Px. FC
Mn (ppm)
Fo content
(b)
Px. FC
Pd. FC
Ni (ppm)
Fo content
(c)
Pd. FC
Px. FC
Ca (ppm)
Fo content

Fig. 7. Mn, Ni, and Ca vs. Fo contents in olivines. The black and green dotted lines represent the modeled fractional crystallization (FC) path from peridotitic (Pd.) and pyroxenitic (Px.) melts at 7kbar. Other various dots indicate mid-ocean ridge basalts (MORB; Sobolev et al., 2007), ocean island basalts (OIB; Rasmussen et al., 2020; Reinhard et al., 2016; Sobolev et al., 2007), large igneous province (LIP; Sobolev et al., 2007), continental rift (Foley et al., 2011; Sobolev et al., 2007), and Cenozoic basalts in East Asia (North China; Li et al., 2016, Hainan; Gu et al., 2019), respectively.

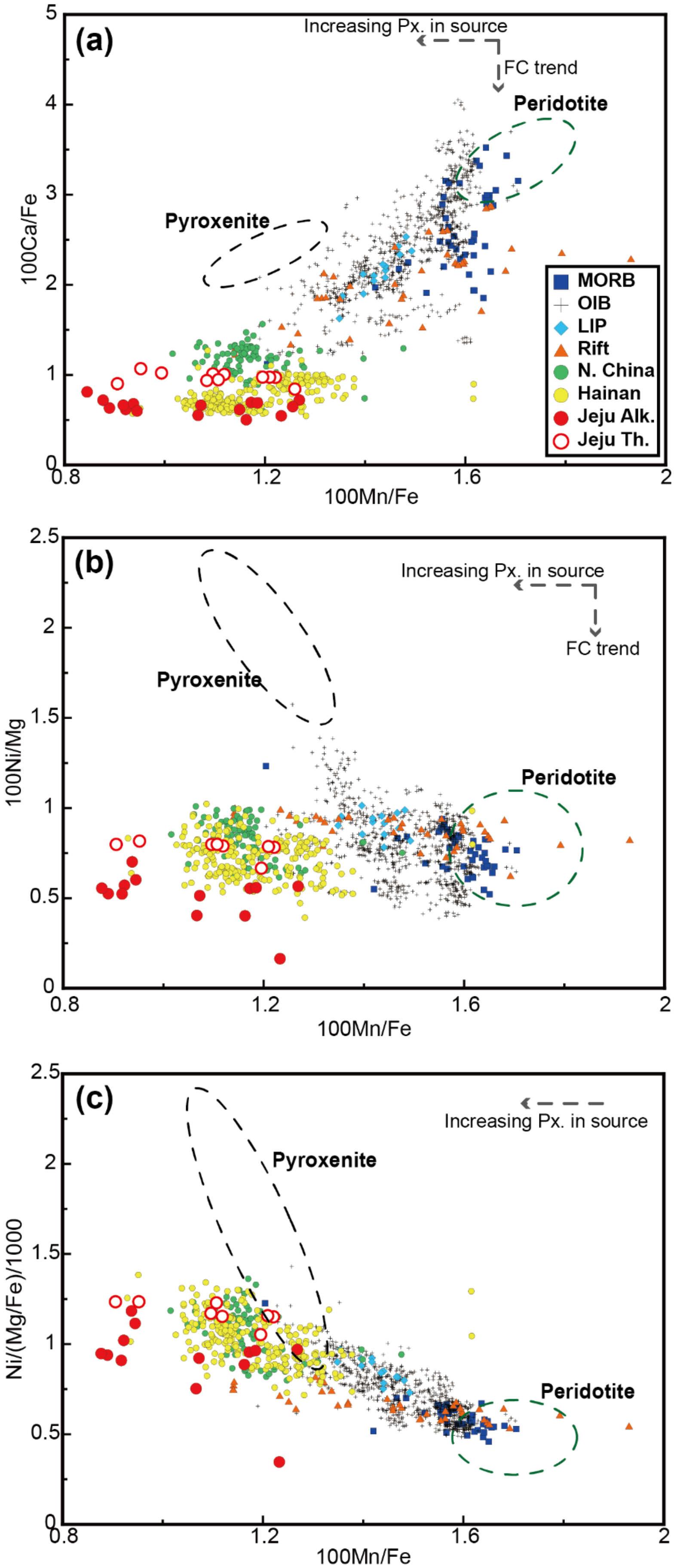

(a)
Increasing Px. in source
FC trend
Peridotite
Pyroxenite
MORB
OIB
LIP
Rift
N. China
Hainan
Jeju Alk.
Jeju Th.
100Ca/Fe
100Mn/Fe
(b)
Increasing Px. in source
FC trend
Pyroxenite
Peridotite
100Ni/Mg
100Mn/Fe
(c)
Increasing Px. in source
Pyroxenite
Peridotite
Ni/(Mg/Fe)/1000
100Mn/Fe

800

Fig. 8. 100Ca/Fe, 100Ni/Mg, and Ni/(Mg/Fe)/1000 vs. 100*Mn/Fe in olivine. The 100*Mn/Fe ratios of the Jeju olivines are similar to the olivines derived from the pyroxenitic melt. The black and green dotted circles mean the equilibrated olivine compositions from the peridotite and pyroxenite derived melts (Sobolev et al., 2007). Other various dots are from references in Fig. 7. **(a)** The 100Ca/Fe ratios of olivined from Jeju Island are relatively low, reflecting fractional crystallization (FC). **(b)** The 100Ni/Mg ratios of the Jeju Island olivines also show lower ratios (<1), caused by fractional crystallization **(c)** the Ni/(Mg/Fe)/1000 and 100*Mn/Fe ratios corrected for the fractional crystallization effect, and the area of the olivines from Jeju Island is close to the pyroxenite range.

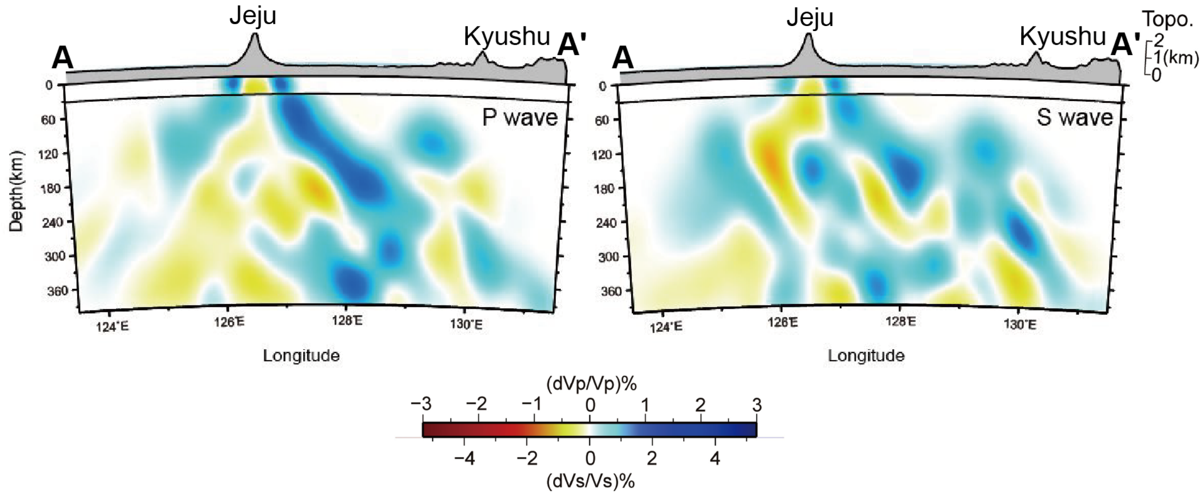

Fig. 9. Vertical cross-sections of the P wave and S wave tomography along the A-A' transect in Fig 1a. Focused low-velocity zone is observed beneath Jeju Island, indicating the asthenospheric upwelling interacting with the SCLM. The relatively thick and cold cratonic lithosphere is located around Jeju Island. Detailed information of the mantle tomography is described in Song et al. (2020). The velocity perturbation scale is shown at the bottom.

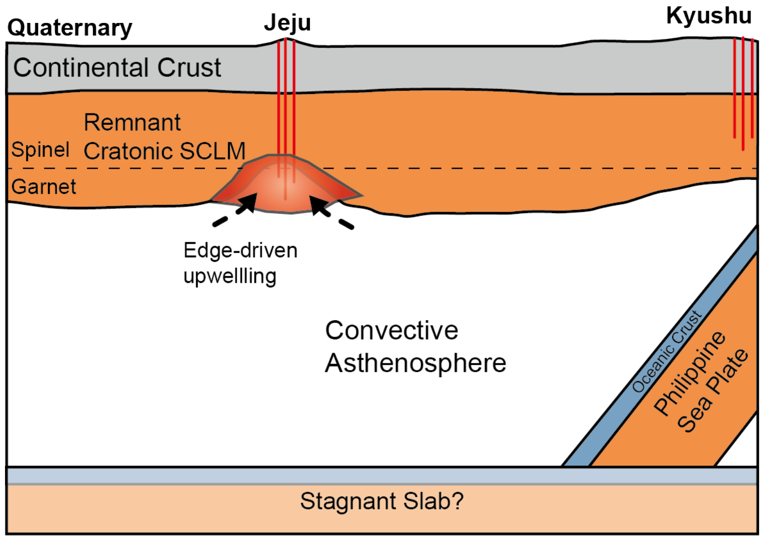

Fig. 10. Schematic illustration for the magma formation of Jeju Island. The remnant cratonic SCLM is located in the east, west, and north of Jeju Island, a possible reservoir of the enriched components. Localized asthenosphere upwelling (e.g., edge-driven convection) could melt the pyroxenitic segregates in the lowermost SCLM. Interaction between the pyroxenite segregates contained in the SCLM and the depleted asthenosphere might generate the magma of Jeju Island.